J|A|C|S
ARTICLES
Published on Web 04/06/2004

Structural, Spectroscopic, and Computational Study of an Octahedral, Non-Heme $\{Fe-NO\}^{6-8}$ Series: $[Fe(NO)(cyclam\text{-}ac)]^{2+/+/0}$

Ricardo García Serres, Craig A. Grapperhaus,† Eberhard Bothe, Eckhard Bill, Thomas Weyhermüller, Frank Neese,* and Karl Wieghardt*

Contribution from the Max-Planck-Institut für Bioanorganische Chemie, Stiftstrasse 34-36, D-45470 Mülheim an der Ruhr, Germany

Received December 3, 2003; E-mail: wieghardt@mpi-muelheim.mpg.de

Abstract: The reaction of low-spin $[Fe^{II}Cl(cyclam\text{-}ac)]$ with NO in CH_3CN yields the octahedral, non-heme (nitrosyl)iron complex $[Fe(NO)(cyclam\text{-}ac)](PF_6)$ (**2**), $S = {}^1/_2$, which can be one-electron oxidized with (tris(4-bromophenyl)ammoniumyl)hexachloroantimonate to the complex $[Fe(NO)(cyclam\text{-}ac)](PF_6)_2$ (**1′**), $S = 0$, or complex $[Fe(NO)(cyclam\text{-}ac)]Cl(ClO_4)\cdot H_2O$ (**1**); $(cyclam\text{-}ac)^-$ represents the pentadentate monoanion of 1,4,8,11-tetraazacyclotetradecane-1-acetic acid. Similarly, in CH_3CN solution **2** can be electrochemically or chemically reduced by one-electron to the neutral complex $[Fe(NO)(cyclam\text{-}ac)]^0$ (**3**), $S = 0$. **1**−**3** represent members of the $\{FeNO\}^{6-8}$ series, respectively. The electronic structure of these three species have been spectroscopically elucidated by EPR, UV−vis, Mössbauer, and IR spectroscopy. The crystal structures of **1** and **2** have been determined by X-ray crystallography. In addition, detailed density functional calculations have been performed for all three species taking into account the possibility that **3** is actually a protonated HNO or NOH species. For all complexes structures, energetics, IR parameters, and Mössbauer parameters as well as EPR parameters (*g*-values and hyperfine couplings) have been calculated using state-of-the art DFT methods which are compared to experiment. The results establish unequivocally that **3** is indeed the elusive $\{FeNO\}^8$ species. Furthermore a detailed picture of the bonding in the low-spin non-heme iron nitrosyl series $\{FeNO\}^6$, $\{FeNO\}^7$, and $\{FeNO\}^8$ has been developed. This allows a description of **1** as a low-spin ferrous complex containing an N-coordinated NO^+, whereas **2** is a low-spin ferrous species with a $NO^\bullet$ ligand and **3** is a low-spin ferrous complex with a coordinated NO^-. On the basis of this description, all spectroscopic and geometric observables find a satisfactory interpretation.

Introduction

It is well-known that mononuclear, octahedral, non-heme (nitrosyl)iron complexes exist either as diamagnetic $\{Fe-NO\}^6$ ($S_t = 0$), paramagnetic $\{Fe-NO\}^7$ ($S_t = {}^1/_2$ or ${}^3/_2$), or diamagnetic $\{Fe-NO\}^8$ ($S_t = 0$) species according to the nomenclature introduced by Enemark and Feltham.[1] The electronic structure of $\{Fe-NO\}^7$ ($S_t = {}^3/_2$) species has been experimentally established by X-ray crystallography, X-ray absorption, resonance Raman, Mössbauer, and EPR spectroscopy in conjunction with SCF-Xα-SW[2a] and GGA density functional[2b] calculations; they are described as high-spin ferric (d^5) species antiferromagnetically coupled to an NO^- ($S = 1$) ligand yielding the observed $S_t = {}^3/_2$ ground state.[2−5] More recently, complexes of the type $\{Fe-NO\}^7$ ($S = {}^1/_2$) have been described as low-spin ferrous (d^6) species containing a coordinated $NO^\bullet$ radical.[6−9] On the other hand, we have recently proposed[10] that the Mössbauer parameters of *trans*-$[Fe(NO)Cl(cyclam)]PF_6$, an $\{Fe-NO\}^7$ ($S_t = {}^1/_2$) species, allow the description of its electronic structure as intermediate-spin ferric ($S_{Fe} = {}^3/_2$) coupled antiferromagnetically to an NO^- anion ($S_{NO^-} = 1$).

In contrast, $\{Fe-NO\}^8$ species are exceedingly rare and their electronic structure has not been investigated in detail. We had reported[10] that *trans*-$[Fe(NO)Cl(cyclam)](ClO_4)$ ($S_t = {}^1/_2$) can be electrochemically reversibly reduced by one electron yielding

† Present address: Department of Chemistry, University of Louisville, Louisville, KY 40292.

(1) (a) Enemark, J. H.; Feltham, R. D. *Coord. Chem. Rev.* **1974**, *13*, 339. (b) Feltham, R. D.; Enemark, J. H. In *Topics in Inorganic and Organometallic Stereochemistry*; Geoffroy, G., Ed.; Éliel, E. L., Allinger, N. L., Vol. Eds.; Wiley & Sons: New York, 1981; Vol. 12, *Topics in Stereochemistry*. (c) Westcott, B. L.; Enemark, J. H. In *Inorganic Electronic Structure and Spectroscopy*; Solomon, E. I., Lever, A. B. P., Eds.; Wiley & Sons: New York, 1999; Vol. II, p 403.
(2) (a) Zhang, Y.; Pavlosky, M. A.; Brown, C. A.; Westre, T. E.; Hedman, B.; Hodgson, K. O.; Solomon, E. I. *J. Am. Chem. Soc.* **1992**, *114*, 9189. (b) Rodriguez, J. H.; Xia, Y.-M.; Debrunner, P. *J. Am. Chem. Soc.* **1999**, *121*, 7846.
(3) Noodleman, L.; Baerends, E. J. *J. Am. Chem. Soc.* **1984**, *106*, 2316.
(4) Brown, C. A.; Pavlosky, M. A.; Westre, T. E.; Zhang, Y.; Hedman, B.; Hodgson, K. O.; Solomon, E. I. *J. Am. Chem. Soc.* **1995**, *117*, 715.
(5) Westre, T. E.; Di Cicco, A.; Filipponi, A.; Natoli, C. R.; Hedman, B.; Solomon, E. I.; Hodgson, K. O. *J. Am. Chem. Soc.* **1994**, *116*, 6757.
(6) Wanner, M.; Scheiring, T.; Kaim, W.; Slep, L. D.; Baraldo, L. M.; Olabe, J. A.; Zális, S.; Baerends, E. J. *Inorg. Chem.* **2001**, *40*, 5704.
(7) Sellmann, D.; Blum, N.; Heinemann, F. W.; Hess, B. A. *Chem.—Eur. J.* **2001**, *7*, 1874.
(8) Li, M.; Bonnet, D.; Bill, E.; Neese, F.; Weyhermüller, T.; Blum, N.; Sellmann, D.; Wieghardt, K. *Inorg. Chem.* **2002**, *41*, 3444.
(9) López, J. P.; Heinemann, F. W.; Prakash, R.; Hess, B. A.; Horner, O.; Jeandey, C.; Oddou, J.-L.; Latour, J.-M.; Grohmann, A. *Chem.—Eur. J.* **2002**, *8*, 5709.
(10) Hauser, C.; Glaser, T.; Bill, E.; Weyhermüller, T.; Wieghardt, K. *J. Am. Chem. Soc.* **2000**, *122*, 4353.

10.1021/ja030645+ CCC: $27.50 **© 2004 American Chemical Society**

Chart 1. Possible Electronic Structure Descriptions of {FeNO}$^{6-8}$ Species

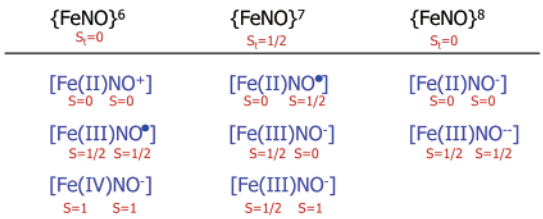

the neutral complex [Fe(NO)Cl(cyclam)]^0 ($S_t = 0$). The electronic and zero-field Mössbauer spectra have been reported,[10] and it was concluded that the reduction was ligand- rather than metal-centered. The interpretation of the spectroscopy was based on the assumption that the chloro ligand remained coordinated in solution upon reduction and did not exchange with a solvent molecule (acetonitrile) or that reoxidation to the starting material or its acetonitrile derivative [Fe(NO)(cyclam)-(CH_3CN)]$^{2+}$ had not occurred. As we will show, these assumptions do not hold.

Here we have synthesized the pendent arm macrocycle 1,4,8,11-tetraazacyclotetradecane-1-acetic acid (cyclam-acH)[11] and its (nitrosyl)iron complex [Fe(NO)(cyclam-ac)](PF_6) (**2**) because it was hoped that upon one-electron oxidation or reduction the O-coordinated carboxylate would not dissociate.

The electronic structure of iron nitrosyls has been under dispute for a long time (vide infra). For the {FeNO}^{6} form a description $Fe^{IV}NO^-$ was proposed on the basis of Mössbauer data.[10] The {FeNO}^{7} state in the $S = {}^3/_2$ spin state has been proposed to be best described as high-spin Fe(III) ($S = {}^5/_2$) antiferromagnetically coupled to NO^- ($S = 1$).[2a,4,5] The analoguous situation in the $S = {}^1/_2$ {FeNO}^{7} form is less clear, but recent papers have formulated it as being best described as $Fe^{II}NO^{\bullet}$.[6,8,9,12-14] The {FeNO}^{8} species is elusive. A recent paper on the species $[Fe(CN)_5(NO)]^{4-}$ which has first been observed by Hemmerich has described it as Fe(II)NO^- (closed shell),[13] which is in agreement with the species [Fe(porph)(NO)(NH_3)]$^-$ that we have investigated as a model for a reaction intermediate of cytochrome *c* nitrite reductase (CCNIR).[15] Chart 1 puts the different limiting descriptions of the three low-spin states into perspective. In this paper, a detailed experimental and theoretical study of the series [Fe(cyclam-acetate)(NO)]$^{2+,+,0}$ is described. Experimentally calibrated electronic structure calculations will be used to arrive at an interpretation of the series in terms of limiting valence descriptions. The results provide strong evidence for essentially ligand-centered reduction steps with important consequences for the chemical properties and the reactivity of the bound NO ligand and are in agreement with a recent theoretical study on the iron−pentacyano−NO system.[13]

Experimental Section

1. Syntheses. Caution! *Although no explosion was encountered in this work, perchlorate salts could detonate upon heating and should be handled with caution and in small amounts.*

The ligand 1,4,8,11-tetraazacyclotetradecane-1-acetic acid tetrahydrochloride and [Fe^{III}Cl(cyclam-ac)](PF_6) have been prepared according to published procedures.[11,16]

[Fe(NO)(cyclam-ac)](PF_6) (2). To a solution of [Fe^{III}Cl(cyclam-ac)](PF_6) (0.246 g; 0.5 mmol) in degassed, freshly distilled acetonitrile (35 mL) under an argon blanketing atmosphere was added dropwise (Hamilton Syringe) a 1.0 M solution (0.7 mL) of lithium triethylborohydride in dry tetrahydrofuran at 0 °C. The mixture was stirred at 0 °C under Ar for 10 min during which time the color of the solution changed from dark (bordeaux) red to light orange. NO was slowly bubbled through the cold solution for 5 min. An immediate color change to deep red occurred. The solution was allowed to warm up to ambient temperature and purged with Ar. An Ar flow was maintained over the solution for several hours to slowly reduce the reaction volume to 5 mL by evaporation of the solvent. Then 15 mL of degassed CH_3OH was added to the slurry with a syringe taking care that two liquid phases prevail. Under a slow constant Ar flow the solvent was allowed to evaporate. After 24 h dark red crystals of **2** suitable for single-crystal X-ray crystallography were collected by filtration. Yield: 0.16 g (66%). Anal. Calcd for $C_{12}H_{25}N_5O_3FePF_6$: C, 29.52; H, 5.16; N, 14.35. Found: C, 29.7; H, 5.4; N, 14.2. UV−vis [CH_3CN (0.10 M [N(*n*-Bu)$_4$]PF_6)]: 220 nm (1.4×10^4 M^{-1} cm^{-1}), 395 (700), 540 (230).

[Fe(NO)(cyclam-ac)](ClO_4)Cl·H_2O (1). To a solution of **2** (0.098 g; 0.20 mmol) in degassed acetonitrile (10 mL) was added at ambient temperature with stirring (tris(4-bromophenyl)ammoniumyl)hexachloroantimonate (83 mg; 0.20 mmol). After the combination was stirring for 5 min, a light yellow solution was obtained from which colorless tris(4-bromophenyl)amine precipitated, which was filtered off. After addition of tetra-*n*-butylammonium perchlorate (0.20 g; 0.6 mmol) dissolved in degassed CH_3CN (5 mL), the solvent was allowed to evaporate slowly by passing a slow flow of Ar through the solution. After 12 h a yellow solid was collected by filtration and redissolved in water (5 mL). From the filtered solution yellow crystals of **1** were obtained after slow evaporation of water. Yield: 95 mg (72%). Anal. Calcd for $C_{12}H_{27}N_5O_8FeCl_2$: C, 29.05; H, 5.49; N, 14.12. Found: C, 28.8; H, 5.5; N, 13.9. UV−vis [CH_3CN (0.10 M [N(*n*-Bu)$_4$]PF_6)]: 220 nm (1.6×10^4 M^{-1} cm^{-1}), 351 sh (800), 430 sh (170).

Synthesis of [Fe(NO)(cyclam-ac)] (3) in Solution for Mössbauer Measurements. A solution of **2** (25 mg; 51 μmol) in degassed, freshly distilled CH_3CN (0.5 mL) was placed in a Schlenk tube with stirring and Ar circulation. With a syringe, a solution of cobaltocene (18 mg) in dry, degassed toluene (0.5 mL) was added. The combined solutions were transferred with a syringe into a Mössbauer sample holder which was placed in another Schlenk tube under Ar. The bottom of this Schlenk tube was immersed in liquid N_2. The solution in the Mössbauer sample holder froze within a few minutes. The tube was opened, and the probe was stored in liquid N_2. Samples prepared in this fashion contained in general more reduced **3** (~40%) than samples prepared electrochemically via controlled-potential electrolysis. Complex **3** is very air sensitive. UV−vis [CH_3CN (0.10 M [N(*n*-Bu)$_4$]PF_6)]: 220 nm (1.0×10^4 M^{-1} cm^{-1}), 440 sh (300), 590 sh (150).

Synthesis of Isotopomers of 1−3. The following isotopomers have been synthesized: ^{57}Fe-enriched samples of **1** and **2** and **3** by using $^{57}FeCl_3$ and [^{57}FeCl(cyclam-ac)](PF_6). By using commercially available $^{15}N^{18}O$ for the synthesis of **2** the isotopomer [Fe($^{15}N^{18}O$)(cyclam-ac)](PF_6) has been obtained which was converted to [Fe($^{15}N^{18}O$)-(cyclam-ac)]$^{2+}$ in solution by one-electron oxidation and, similarly, to [Fe($^{15}N^{18}O$)(cyclam-ac)]^0 by reduction of labeled **2** with 1 equiv of cobaltocene. Labeling of the N−H groups of cyclam-ac ligand with deuterium was achieved via dissolution of **2** in D_2O.

2. Physical Measurements. The equipment used for IR, UV−vis, Mössbauer, and EPR spectroscopy and magnetochemistry has been

(11) Studer, M.; Kaden, T. *Helv. Chim. Acta* **1986**, *69*, 2081.
(12) Rovira, C.; Kunc, K.; Hutter, J.; Ballone, P.; Parinello, M. *J. Phys. Chem. A* **1997**, *101*, 8914.
(13) Lebrero, M. C. G.; Scherlis, D. A.; Estiu, G. L.; Olabe, J. A.; Estrin, D. A. *Inorg. Chem.* **2001**, *40*, 4127.
(14) Patra, A.; Rowland, J. M.; Marlin, D. S.; Bill, E.; Olmstead, M. M.; Mascharak, P. *Inorg. Chem.* **2003**, *42*, 6812.
(15) Einsle, O.; Messerschmidt, A.; Huber, R.; Kroneck, P. M. H.; Neese, F. *J. Am. Chem. Soc.* **2002**, *124*, 11737.
(16) Grapperhaus, C. A.; Mienert, B.; Bill, E.; Weyhermüller, T.; Wieghardt, K. *Inorg. Chem.* **2000**, *39*, 5306.

described previously in ref 17. Low-temperature EPR, magnetic Mössbauer spectra, and magnetization measurements were analyzed on the basis of a spin-Hamiltonian description of the electronic ground-state spin multiplet as is described in detail in ref 17. The EPR line shapes for compound **2** were taken as Gaussians with widths σ according to a *g*- and *A*-strain model with

$$\sigma(M_I) = \{W_f^2 g^{-2} + \sum_{i=x,y,z} [W_i^2 + (c_{1i}\nu + c_{2i}M_I)^2] l_i^2\}^{1/2}$$

where l_i are direction cosines, M_I are magnetic quantum numbers of the nuclear spin, g is the orientation-dependent g-factor, W_f and W_i are the frequency- and orientation-dependent parts of the intrinsic line width, ν is the spectrometer frequency, and c_1 and c_2 are the strain parameters.

Infrared spectra were recorded on a Perkin-Elmer FT-IR/NIR 2000 spectrophotometer. IR spectra of solid samples were measured in KBr pellets whereas solution spectra were recorded between NaCl windows with varying path-length spacers or in a thermostated optically transparent thin layer electrode (OTTLE) cell with CaF_2 windows.

3. X-ray Crystallographic Data Collection and Refinement of the Structures. A yellow single crystal of **1** and a dark red crystal of **2** were coated with perfluoropolyether, picked up with a glass fiber, and mounted in the nitrogen cold stream of the diffractometers operating at 100 K. Intensity data were collected using a Nonius Kappa-CCD diffractometer equipped with a Mo-target rotating-anode X-ray source in case of compound **1** and a Siemens SMART-CCD diffractometer with a fine focus sealed Mo X-ray tube for **2**. A graphite monochromator was used in both cases (Mo Kα radiation, $\lambda = 0.710\ 73$ Å). Final cell constants were obtained from least-squares fit of subsets of several thousand intense reflections. Intensity data for compound **2** were corrected for absorption using the semiempirical program SADABS,[18] whereas those of **1** were left uncorrected. Crystallographic data for the compounds are listed in the Supporting Information (Tables S1−S10). The Siemens ShelXTL[19] software package was used for solution and artwork of the structure, and ShelXL97 was used for the refinement.[20] The structures were readily solved by direct and Patterson methods and subsequent difference Fourier techniques. All non-hydrogen atoms were refined anisotropically, and hydrogen atoms were placed at calculated positions and refined as riding atoms with isotropic displacement parameters. The NO ligand in **2** was found to be disordered by rotation over two sites. The position of the oxygen atom O(5) was split in a 70:30 ratio.

4. Molecular Orbital Calculations. All calculations were carried out with the program package ORCA[23] except for the geometry relaxation step which was carried out in internal coordinates according to von Arnim and Ahlrichs[24] through an interface of ORCA to the "relax" and "define" modules of the TurboMole 5.2 package.[25] The structures of all molecules were fully geometry optimized with the BP86 functional[26] and the TZVP basis set.[27] The resolution of the identity approximation was employed,[28] and the auxiliary basis sets used were those developed by Eichkorn et al.[28c,d] Harmonic frequencies were calculated through two sided numerical differentiation of analytic gradients at the BP86/TZVP level using an increment of 0.005 bohr. No negative frequencies were observed for any of the molecules thus proving their identity as (possibly local) minima. IR intensities were calculated through numerical differentiation of analytically obtained dipole moments. Specific normal modes were assigned on the basis of theoretically calculated isotope shifts and visual inspection. Approximate quasi-diatomic force constants were obtained from the Cartesian force constant matrix **F** by the equation $f_{AB} = -\sum_{\mu,\nu} t_\mu t_\nu F_{A_\mu B_\nu}$ ($\mu,\nu = x,y,z$), where $\boldsymbol{t} = (\boldsymbol{R}_A - \boldsymbol{R}_B)|R_A - R_B|^{-1}$ and $\boldsymbol{R}_A$ and $\boldsymbol{R}_B$ denote the positions of atoms A and B.

Zero-point energies and thermal corrections to the energy were obtained from the frequency calculations. The choice of the BP86 functional is motivated by computational efficiency as well as the observation made by a variety of workers that structural parameters of transition metal complexes predicted at the BP86 level tend to be more accurate than the B3LYP predictions. In addition, harmonic frequencies calculated at the BP86 level tend to be in better agreement with observed fundamentals, which has been shown in ref 29 to arise from a cancellation of the errors.

Solvent effects were treated at the BP86/TZVP level by the COSMO method[30] as implemented in the TurboMole package.[31] A dielectric constant of 78 was used in the calculations; all other COSMO parameters were default values. The atomic radii employed were those optimized for the COSMO method[32] except for iron, where the Bondi radius of 2.223 Å was used.

Electronic energies and properties were calculated at the optimized geometries with the B3LYP functional.[35] In these calculations the flexible CP(PPP) basis set was used for iron,[36] while all other atoms were described with the TZVP basis except for the EPR calculations where the nitrogens were described by the IGLO-III basis.[37] The CP(PPP) basis is based on the Ahlrichs basis sets[27,38] with complete decontraction of the s-part and additional steep s-functions as well as two polarizing sets of p-orbitals with Wachters exponents[39] and a set of f-functions with exponents taken from the TurboMole library.[38] Mössbauer isomer shift (IS) and quadrupole splitting (QS) predictions followed the procedure in ref 36, where a calibration cure has been constructed which relates the calculated electron density at the nucleus to the eperimentally observed IS. It was argued in ref 36 that this calibration does not depend on the type of iron complex studied (valence

(17) Meyer, K.; Bill, E.; Mienert, B.; Weyhermüller, T.; Wieghardt, K. *J. Am. Chem. Soc.* **1999**, *121*, 4859.
(18) Sheldrick, G. M. *SADABS*; Universität Göttingen: Göttingen, Germany, 1994.
(19) *ShelXTL V.5*; Siemens Analytical X-ray Instruments, Inc.: Madison, WI, 1994.
(20) Sheldrick, G. M. *ShelXL97*; Universität Göttingen: Göttingen, Germany, 1997.
(21) (a) Bosnich, B.; Poon, C. K.; Tobe, M. L. *Inorg. Chem.* **1965**, *4*, 1102. (b) Adam, K. R.; Atkinson, I. M.; Lindoy, L. F. *Inorg. Chem.* **1997**, *36*, 480.
(22) Grapperhaus, C. A.; Patra, A. K.; Mashuta, M. S. *Inorg. Chem.* **2002**, *41*, 1039.
(23) Neese, F. *ORCA−an ab initio, DFT and Semiempirical Electronic Structure Package*, version 2.2, revision 46; Max-Planck Institut für Strahlenchemie: Mülheim, Germany, May 2003.
(24) von Arnim, M.; Ahlrichs, R. *J. Chem. Phys.* **1999**, *111*, 9183.
(25) Ahlrichs, R.; Bär, M.; Baron, H. P.; Bauernschmitt, R.; Böcker, S.; Ehrig, M.; Eichkorn, K.; Elliott, S.; Furche, F.; Haase, F.; Häser, M.; Horn, H.; Huber, C.; Huniar, U.; Kattanek, M.; Kölmel, C.; Kollwitz, M.; May, K.; Ochsenfeld, C.; Öhm, H.; Schäfer, A.; Schneider, U.; Treutler, O.; von Arnim, M.; Weigend, F.; Weis, P.; Weiss, H. *TurboMole-Program System for ab initio Electronic Structure Calculations*, version 5.2; Universität Karlsruhe: Karlsruhe, Germany, 2000.
(26) (a) Perdew, J. P. *Phys. Rev. B* **1986**, *33*, 8822. (b) Becke, A. D. *J. Chem. Phys.* **1988**, *84*, 4524.
(27) Schäfer, A.; Huber, C.; Ahlrichs, R. *J. Chem. Phys.* **1994**, *100*, 5829.
(28) (a) Baerends, E. J.; Ellis, D. E.; Ros, R. *Chem. Phys.* **1973**, *2*, 41. (b) Dunlap, B. I.; Connolly, J. W. D.; Sabin, J. R. *J. Chem. Phys.* **1979**, *78*, 3369. (b) Vahtras, O.; Almlöf, J. E.; Feyereisen, M. W. *Chem. Phys. Lett.* **1993**, *213*, 514. (c) Eichkorn, K.; Treutler, O.; Öhm, H.; Häser, M.; Ahlrichs, R. *Chem. Phys. Lett.* **1995**, *242*, 652. (d) Eichkorn, K.; Weigend, F.; Treutler, O.; Ahlrichs, R. *Theor. Chem. Acc.* **1997**, *97*, 119.
(29) Neugebauer, J.; Hess, B. A. *J. Chem. Phys.* **2003**, *118*, 7215.
(30) Klamt, A.; Schuurmann, G. *J. Chem. Soc., Perkin Trans.* **1993**, *2*, 799−805.
(31) Schäfer A.; Klamt, A.; Sattel, D.; Lohrenz, J. C. W.; Eckert, F. *Phys. Chem. Chem. Phys. 2* 2187−2193.
(32) Klamt, A.; Jonas, V.; Burger, T.; Lohrenz, J. C. W. *J. Phys. Chem. A* **1998**, *102*, 5074−5085.
(33) Marchenko, A. V.; Vedernikov, A. N.; Dye, D. F.; Pink, M.; Zaleski, J. M.; Caulton, K. G. *Inorg. Chem.* **2002**, *41*, 4087−4089.
(34) Southern, J. S.; Green, M. T.; Hillhouse, G. L.; Guzei, I. A.; Rheingold, A. L. *Inorg. Chem.* **2001**, *40*, 6039−6046.
(35) (a) Lee, C.; Yang, W.; Parr, R. G. *Phys. Rev. B* **1988**, *37*, 785. (b) Becke, A. D. *J. Chem. Phys.* **1993**, *98*, 5648.
(36) Neese, F. *Inorg. Chim. Acta* **2002**, *337*, 181.
(37) Kutzelnigg, W.; Fleischer, U.; Schindler, M. In *NMR basic principles and progress*; Diehl, P., Fluck, E., Günther, H., Kosfield, R., Seeling, J., Eds.; Springer: Heidelberg, Germany, 1990; Vol. 23.
(38) Basis sets were obtained from the ftp server of the quantum chemistry group at the University of Karlsruhe (Karlsruhe, Germany) under http://www.chemie.uni-karlsruhe.de/PC/TheoChem/.
(39) (a) Wachters, A. J. H. *J. Chem. Phys.* **1970**, *52*, 1033. (b) Hay, P. J. *J. Chem. Phys.* **1977**, *66*, 4377.

state, spin state, total charge, or coordination number). For the quadrupole moment of ^{57}Fe the value 0.15 barn was used.[40] EPR properties were predicted using coupled perturbed Kohn−Sham theory for the **g**-tensor[41] and the spin−orbit coupling contribution to the hyperfine coupling (HFC) tensor.[42] Fermi contact terms and spin−dipole contributions to the HFC were obtained as expectation values over the B3LYP ground-state spin density.

The natural population analysis of the B3LYP densities was done with the GENNBO package of Weinhold and co-workers.[43] Orbitals and densities were visualized with the Molekel program.[44]

Results, Analyses, and Discussion

1. Preparation and Characterization of Complexes. The octahedral, low-spin ferric complex [Fe^{III}Cl(cyclam-ac)](PF$_6$) ($S = {}^1/_2$) has been described previously.[16] It was used here as a convenient starting material for the synthesis of paramagnetic [Fe(NO)(cyclam-ac)](PF$_6$) (**2**). Electrochemical or chemical one-electron reduction of this monocationic chloro complex yields the neutral, low-spin, yellow ferrous species [Fe^{II}Cl(cyclam-ac)]^0 ($S = 0$). Chemically this reduction is efficiently achieved in CH$_3$CN solution by lithium triethylborohydride. Such solutions react rapidly under an Ar blanketing atmosphere with NO yielding deep red, crystalline [Fe(NO)(cyclam-ac)](PF$_6$) (**2**), which according to the Enemark and Feltham nomenclature[1] is of the {Fe−NO}^{7} type.

Complex **2** possesses an $S = {}^1/_2$ ground state as was deduced from temperature-dependent, magnetic susceptibility measurements (4−300 K) and EPR spectroscopy (see below). The infrared spectrum of solid **2** (KBr disk) exhibits strong bands at 1615 and 1643 cm^{-1}, where the latter is assigned a ν(C═O) stretching frequency of the coordinated carboxylate and the former is the ν(NO) stretch. This band shifts to 1548 cm^{-1} upon isotopic labeling with ^{15}N^{18}O whereas the 1643 cm^{-1} band does not shift. ν(C−H) stretching frequencies are observed as a multiplet at ∼2900 cm^{-1}, and three ν(N−H) bands are observed at 3143, 3266, and 3298 cm^{-1}, which shift upon deuteration to 2433, 2381, and 2328 cm^{-1}.

By using the strong one-electron oxidant (tris(4-bromophenyl)ammoniumyl)hexachloroantimonate, complex **2** can be one-electron oxidized in acetonitrile. Addition of [N(*n*-Bu)$_4$]ClO$_4$ to this solution and recrystallization of the crude precipitate from water yields yellow crystals of [Fe(NO)(cyclam-ac)](ClO$_4$)Cl·H$_2$O (**1**) in good yield. In the infrared spectrum (KBr disk) of [Fe(NO)(cyclam-ac)](PF$_6$)$_2$ (**1′**) the following bands have been identified: ν(NO), 1893 cm^{-1}; ν(C═O), 1703 cm^{-1}; 1670 cm^{-1}; ν(C−O), 1289 cm^{-1}; ν(N−H), 3032 cm^{-1}; ν(C−H), 2851 cm^{-1}. Complexes **1** and **1′** are diamagnetic; they possess an $S = 0$ ground state as is expected for an {Fe−NO}^{6} species.

The neutral species [Fe(NO)(cyclam-ac)] (**3**) has been prepared in CH$_3$CN solution at ambient temperature under an Ar-blanketing atmosphere from **2** with cobaltocene as one-electron reductant according to eq 1.

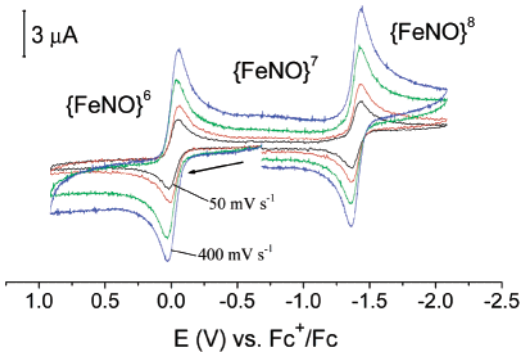

Figure 1. Cyclic voltammogram of **2** in CH$_3$CN at 20 °C (0.10 M [N(*n*-Bu)$_4$]PF$_6$ supporting electrolyte; glassy carbon working electrode; scan rates 50, 100, 200, 400 mV s^{-1}).

It has not been possible to isolate a solid material. Therefore, we have investigated the above (frozen) solutions of **3** by Mössbauer and infrared spectroscopy (vide infra).

$$[\text{Fe(NO)(cyclam-ac)}]^+ + [\text{Cp}_2\text{Co}] \xrightarrow[\text{Ar}]{\text{CH}_3\text{CN}} [\text{Fe(NO)(cyclam-ac)}]^0 + [\text{Cp}_2\text{Co}]^+ \quad (1)$$

2. Electro- and Spectroelectrochemistry. The electrochemistry of **2** in dry CH$_3$CN containing O.10 M [N(*n*-Bu)$_4$]PF$_6$ as supporting electrolyte has been studied by cyclic voltammetry. Figure 1 shows that two reversible one-electron-transfer waves at −0.01 V vs ferrocenium/ferrocene (Fc$^+$/Fc) and at −1.39 V vs Fc$^+$/Fc are observed. Controlled-potential electrolysis at appropriately fixed potentials established that the first wave corresponds to a one-electron oxidation of **2**, whereas the latter is a one-electron reduction as shown in eq 2.

These potentials are very similar to those reported previously for [Fe^{III}(NO)Cl(cyclam)](ClO$_4$).[10] It is interesting that the coulometrically one-electron oxidized as well as the one-electron reduced species are stable in solution for hours at ambient temperature under an Ar-blanketing atmosphere. Figure 2 shows the electronic spectra of **1**−**3**. It is noted that both the oxidation and reduction of **2** are clean, reversible processes. In both cases isosbestic points are observed and the controlled rereduction or reoxidation of **1** and **3**, respectively, yielding **2** produces the complete spectrum of **2** again.

$$\underset{\{\text{Fe−NO}\}^6}{[\text{Fe(NO)(cyclam-ac)}]^{2+}} \underset{+\text{e}}{\overset{-\text{e}}{\rightleftharpoons}} \underset{\{\text{Fe−NO}\}^7}{[\text{Fe(NO)(cyclam)}]^{+}} \underset{+\text{e}}{\overset{-\text{e}}{\rightleftharpoons}} \underset{\{\text{Fe−NO}\}^8}{[\text{Fe(NO)(cyclam-ac)}]^{0}} \quad (2)$$

We have also recorded the infrared spectra of the electrochemical oxidation and reduction products of **2** in an OTTLE cell. Figure 3 shows the spectral changes during the oxidation (top) and reduction (bottom) of **2** whereas Figure 4 shows a comparison of the ν(NO) stretching frequency changes during oxidation and reduction of **2** and its ^{15}N^{18}O isotopomer, respectively.

As one expects, upon oxidation of **2** yielding **1** the ν(NO) stretch shifts to higher energies (1607 → 1904 cm^{-1}) in excellent agreement with the solid-state spectra of **1** and **2**. In contrast, reduction of **2** generating **3** results in an enormous downshift of the ν(NO) stretch from 1607 to 1271 cm^{-1}. This assignment

(40) Dufek, P.; Blaha, P.; Schwarz, K. *Phys. Rev. Lett.* **1995**, *75*, 3545.
(41) Neese, F. *J. Chem. Phys.* **2001**, 11080.
(42) Neese, F. *J. Phys. Chem. A* **2001**, *105*, 4290. (e) Neese, F. *J. Chem. Phys.* **2003**, *117*, 3939.
(43) Glendening, E. D.; Badenhoop, J. K.; Reed, A. E.; Carpenter, J. E.; Bohmann, J. A.; Morales, C. M.; Weinhold, F. *NBO 5.0*; Theoretical Chemistry Institute, University of Wisconsin: Madison, WI, 2001; http://www.chem.wisc.edu/∼nbo5.
(44) Flükiger, P.; Lüthi, H. P.; Portmann, S.; Weber, J. *MOLEKEL 4.0*; Swiss Center for Scientific Computing: Manno, Switzerland, 2000.

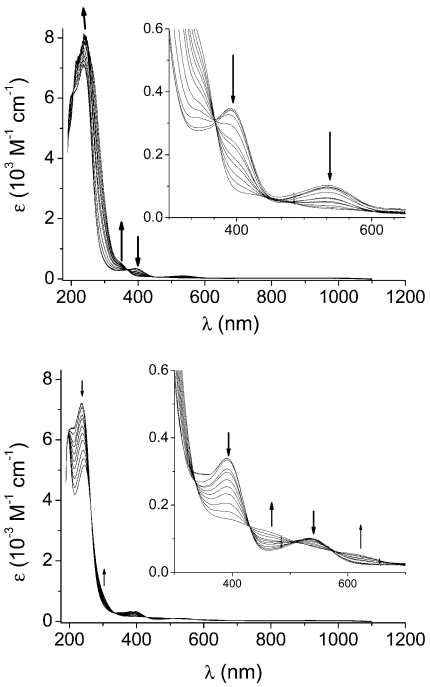

Figure 2. Spectroelectrochemistry of **2** showing the electrochemical oxidation of **2** yielding **1** (top) and its reduction to **3** (bottom) in CH_3CN (0.10 M $[N(n\text{-}Bu)_4]PF_6$) at 0 °C.

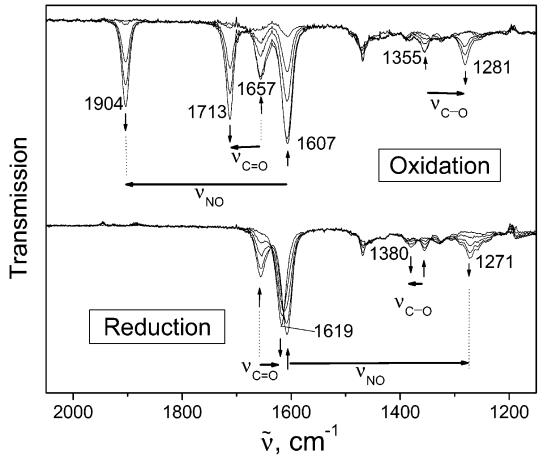

Figure 3. Observed infrared spectral changes during the electrochemical oxidation of **2** (top) and the corresponding reduction of **2** (bottom) at −20 °C in CH_3CN (0.10 M $[N(n\text{-}Bu)_4]PF_6$). Assignments of bands are based on similar experiments using $^{15}N^{18}O$-labeled complex **2**.

is beautifully corroborated by the corresponding shifts in the $^{15}N^{18}O$ isotopomers. The observed isotopic shifts are in good agreement with those calculated using the harmonic model (see Figure 4).

The monodentate carboxylate group in the (cyclam-ac)$^+$ ligand is a sensitive marker for the electronic situation at the central iron ion. Such an O-coordinated carboxylato group gives rise to a ν(C═O) and a ν(C−O) stretching frequency. These are observed in solid **1′** at 1703, 1670, and 1289 cm^{-1} and in solution at 1713 and 1281 cm^{-1}, respectively. In solid **2** these bands are observed at 1642 and 1364 cm^{-1} and in solution at 1657 and 1355 cm^{-1} whereas for **3** in solution these bands are observed at 1619 and 1380 cm^{-1}. These bands do not shift in the $^{15}N^{18}O$ isotopomers. Thus, the difference $\Delta(\nu(C{=}O)-\nu(C{-}O))$ is large at 432 cm^{-1} for **1**, the $\{Fe{-}NO\}^6$ species,

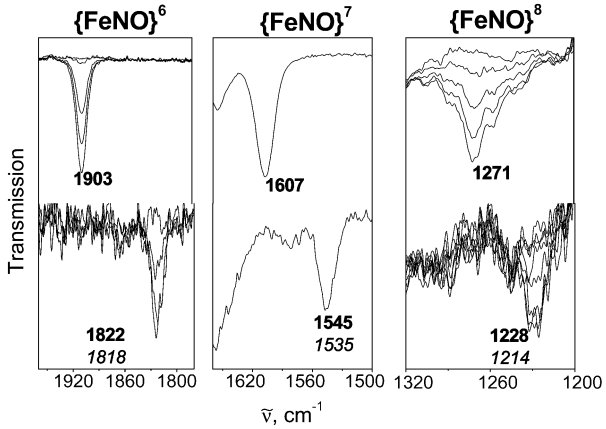

Figure 4. ν(NO) stretching frequencies of complexes **1**−**3** in CD_3CN solution (0.10 M $[N(n\text{-}Bu)_4]PF_6$) (top) and its $^{15}N^{18}O$-labeled isotopomers (bottom). The calculated wavenumbers using the harmonic model are given in italics. Different traces represent different degrees of reduction or oxidation during the electrochemistry.

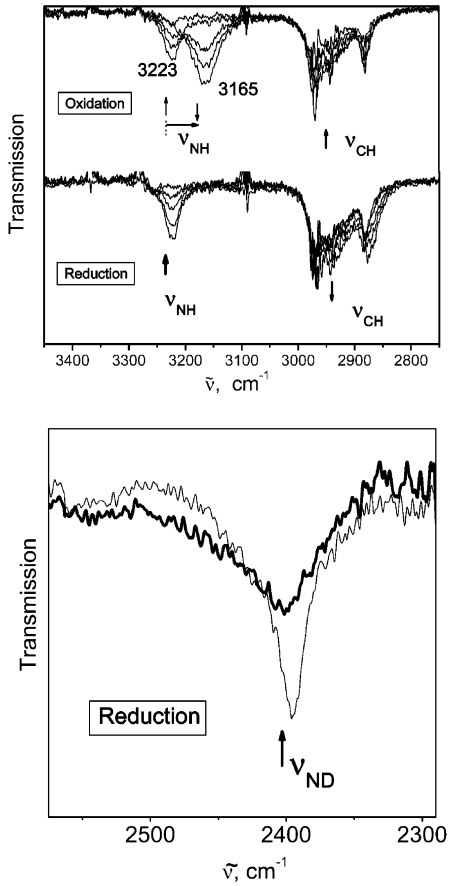

Figure 5. Top: Infrared spectral changes in the ν(C−H) and ν(N−H) regions of oxidized **2** (top) and reduced **2** (bottom) in CD_3CN at −20 °C. Bottom: Infrared spectral changes of the ν(N−D) band during reduction of N−D-labeled **2**.

medium at 302 cm^{-1} for **2**, the $\{Fe{-}NO\}^7$ species, and small at 239 cm^{-1} for **3**, the $\{Fe{-}NO\}^8$ species. It indicates that the $Fe{-}O_{carboxylate}$ bond is the strongest in **1**, medium in **2**, and the weakest in **3**. Note that the $Fe{-}O_{carboxylate}$ bond is always in trans-position with respect to the coordinated nitrosyl ligand.

Finally, Figure 5 exhibits the infrared spectral changes observed in the ν(N−H) and ν(C−H) stretching region. Complex **2** displays a single ν(N−H) stretching frequency at

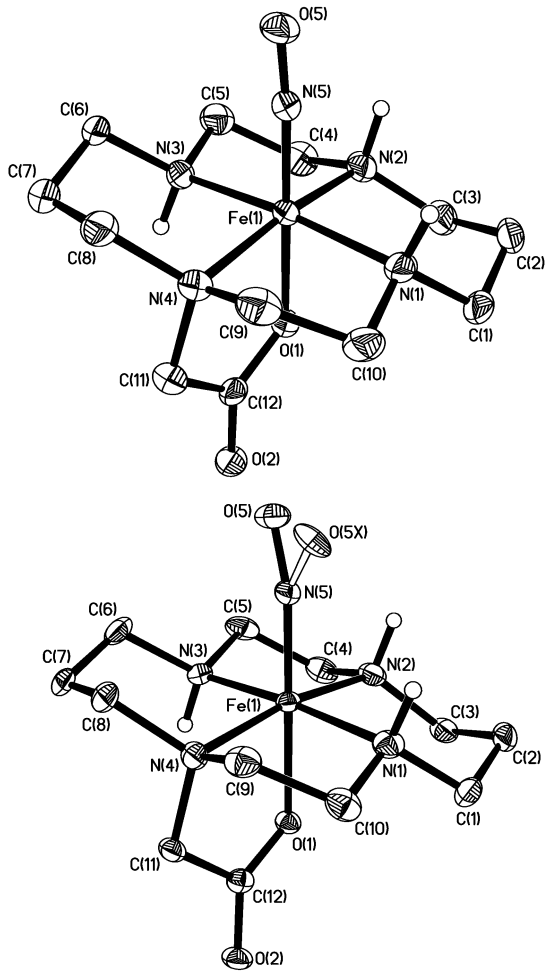

Figure 6. Structure of the dication in crystals of **1** (top) and of the monocation in crystals of **2** (bottom). The two positions of O5 (70%) and O5X (30%) of two conformers in **2** are shown.

3223 cm^{-1} which decreases to 3165 upon oxidation to **1** in CD_3CN solution. The corresponding ν(C−H) bands in the region 2850−3000 cm^{-1} do not shift. Interestingly, the ν(N−H) mode at 3223 of **2** vanishes upon one-electron reduction to **3** apparently without generating a new ν(N−H) stretching mode. If the same experiment is carried out using the deuterated isotopomer of **2** as shown in Figure 5 (bottom), a significant broadening of the ν(N−D) band at 2400 cm^{-1} is observed upon reduction to **3**. We interpret this behavior as a consequence of the decreasing Fe−NO bond angle upon reduction of **2** to **3**. The Fe−NO angle decreases from 149° in **2** to ∼122° in **3** (vide infra). Thereby hydrogen-bonding contacts O···H−N between the nitrosyl and two protons of coordinate cyclam-ac become available in **3** which would broaden the ν(N−H) and ν(N−D) stretching modes.

3. Crystal Structures of 1 and 2. The crystal structure of the {Fe−NO}^{6} species **1** has been determined by single-crystal X-ray crystallography at 100 K as has the structure of the {Fe−NO}^{7} species **2**. Figure 6 shows the structure of the dication in crystals of **1** and of the monocation in crystals of **2** (experimental distances are given together with calculated ones in section 6.A) The cyclam part of the ligand is bound in its strain-free *trans*-III configuration to the central iron ion in both cases;[21] the pending acetato arm is O-coordinated to the iron ion, and in trans position to this group is a nitrosyl ligand in both cases. Thus, the cations in **1** and **2** differ by one electron only.

The NO ligand in **2** is disordered (as in nearly all crystallographically determined structures of {Fe−NO}^{7} (S_t = $^1/_2$) complexes). Two sites with occupancy factors of 70% and 30% have been successfully refined. It is noted that the crystal structure of $[Fe(NO)(pyN_4)]^{2+}$, an {Fe−NO}^{7} (S_t = $^1/_2$) species, does not show this disorder. Thus, the N−O distance of 1.175(8) Å, the Fe−$N_{nitrosyl}$ distance at 1.737(6) Å, and the Fe−N−O bond angle of 139.4(5)° are more trustworthy.[9]

The FeNO group in **1** is nearly linear but bent in **2** (α(FeNO) 175° vs ∼148°). This has also been observed in Sellmann's compounds $[Fe(NO)(pyS_4)]^{0/+}$ and, similarly, in Grohmann's pair $[Fe(NO)(pyN_4)]^{0/+}$.[7,9] As shown in Table 1 the Fe−N bond distance of the coordinated nitrosyl group is always significantly shorter in {Fe−NO}^{6} complexes (∼1.65 Å) than in their corresponding reduced species {Fe−NO}^{7} (∼1.72 Å). It is also significant that the Fe−O bond in **1** at 1.883(3) Å is significantly shorter than in **2** at 2.012(3) Å. This is clearly due to the fact that in **1** the excellent π acceptor NO^+ ligand is in trans position relative to this oxygen which can act as π donor but in **2** a weaker $^{\bullet}$NO ligand is present with reduced π-acceptor capabilities.

4. Mössbauer Spectroscopy. Zero-field Mössbauer spectra on solid samples of **1** and **2** and a frozen CH_3CN solution of **3** have been recorded at 80 K. All compounds show symmetric quadrupole doublets. The absence of magnetic hyperfine splittings shows fast electronic spin relaxation with respect to the nuclear precession rates. In this regime the internal fields at the nuclei average to zero without externally applied fields. The obtained zero-field quadrupole spectra were simulated with Lorentzian doublets; the results are summarized in Table 2. Zero field spectra of **1**−**3** in frozen CH_3CN at 80 K are shown in Figure S1.

Complex **3** was generated by chemical reduction of **2** with cobaltocene in CH_3CN. This complex is air and moisture sensitive and is partially reoxidized during transfer of the solution to the Mössbauer sample holder. Thus, the recorded spectrum contains 60% of **2** and only 40% of **3**.

The isomer shift parameters for the {Fe−NO}^{7} (S_t = $^1/_2$) species $[Fe(NO)Cl(cyclam)]^+$, $[Fe(NO)(pyS_4)]^0$, and **2** are observed in the narrow range 0.26−0.33 mm s^{-1} irrespective of the coligands of the Fe−NO moiety.[8] The same holds true for the {Fe−NO}^{6} (S_t = 0) species $[Fe(NO)Cl(cyclam)]^{2+}$, $[Fe(NO)(pyS_4)]^{1+}$, and **1** (range 0.01−0.04 mm s^{-1}).[8,10] It is therefore unexpected that the isomer shift of **3** at 0.41 mm s^{-1} differs significantly from that reported previously for $[Fe(NO)Cl(cyclam)]^0$ at 0.27 mm s^{-1}.[10] We take this as an indication that the spectrum recorded for the latter species may be flawed by air oxidation of the {Fe−NO}^{8} species to an {Fe−NO}^{7} form which lacks the chloride ligand. It is significant that the one-electron reduction of **2** to the corresponding {Fe−NO}^{8} species **3** is accompanied by a relatively small change of the isomer shift of 0.15 mm s^{-1}. On the other hand, oxidation of **2** to **1** involves an isomer shift change of 0.25 mm s^{-1} which has previously been erroneously interpreted as a metal-centered process. We have later shown that a change of the π-acceptor capabilities of a coordinated NO^+ vs its reduced $NO^{\bullet}$ form brings about an isomer shift change as large as 0.29 mm s^{-1} [8] in the series $[Fe^{II}(NO)^+(pyS_4)]^{1+}$ (δ = 0.04 mm s^{-1}),

Table 1. Comparison of Structural Parameters of Octahedral {FeNO}^{6,7} Complexes and ν(NO) Stretching Frequencies[a]

	{FeNO}^{6}(**1**)	{FeNO}^{7}(**2**)	{FeNO}^{6}(**A**)	{FeNO}^{7}(**B**)	{FeNO}^{6}(**A′**)	{FeNO}^{7}(**B′**)	{FeNO}^{6}(**A″**)
Fe−N, Å	1.663(4)	1.722(4)	1.634(3)	1.712(3)		1.737(6)	1.609(6)
N−O, Å	1.132(5)	1.166(6)	1.141(3)	1.158(6)		1.175(8)	1.167(6)
Fe−N−O, deg	175.5(3)	148.7(4)	179.5(3)	150.4(9)		139.4(5)	177.2(6)
ν(N═O), cm^{-1}	1904	1615	1893	1670	1926	620	1856

[a] Complexes: **A** = [Fe(NO)(′pyS$_4$′)]PF$_6$ and **B** = [Fe(NO)(′pyS$_4$′)]·2CH$_2$Cl$_2$ (ref 7); **A′** = [Fe(NO)(pyN$_4$)]Br$_3$ and **B′** = [Fe(NO)(′pyN$_4$′)]Br$_2$ (ref 9); **A″** = [Fe(NO)(bmmp-TASN)]BPh$_4$ (ref 18). Abbreviations: ′pyS$_4$′ = 2,6-bis(2-mercaptophenylthiomethyl)pyridine(2−); ′ pyN$_4$′ = 2,6-(C$_5$H$_3$N)[CMe(CH$_2$NH$_2$)$_2$]$_2$; (bmmp-TASN)$^{2-}$ = 4,7-bis(2′-methyl-2′-mercaptopropyl)-1-thia-4,7-diazacyclononane.

Table 2. Zero-Field Mössbauer Parameters of Complexes

complex	n in {FeNO}^{n}	T, K	S_t[a]	δ, mm s^{-1} [b]	ΔE_Q, mm s^{-1} [c]	ref
1	6	80	0	0.01	+1.76	this work
2	7	80	1/2	0.26	+0.74	this work
3	8	80	0	0.41	+1.69	this work
[Fe^{III}Cl(cyclam-ac)]$^+$		80	1/2	0.28	+2.66	16
[Fe^{II}Cl(cyclam-ac)]^0		80	0	0.56	+0.52	16
trans-[Fe(cyclam)(NO)Cl]$^+$	7	4.2	1/2	0.27	+1.26	10
trans-[Fe(cyclam)(NO)Cl]$^{2+}$	6	4.2	0	0.04	+2.05	10
trans-[Fe(cyclam)(NO)Cl]^0	8	4.2	0	0.27	+0.77	10[d]
[Fe(NO)(pyS$_4$)]^0 [e]	7	4.2	1/2	0.33	−0.40	8
[Fe(NO)(pyS$_4$)]$^+$	6	4.2	0	0.04	−1.63	8
[Fe(CO)(pyS$_4$)]^0		4.2	0	0.19	+0.88	8
[Fe(PR$_3$)(pyS$_4$)]		4.2	0	0.34	+0.69	8
[Fe(NO)(pyN$_4$)]$^{2+}$	7	77	1/2	0.31	+0.84	9
[Fe(NO)(pyN$_4$)]$^{3+}$	6	77	0	0.04	+1.84	9

[a] Ground state. [b] Isomer shift vs α-Fe at 298 K. [c] Quadrupole splitting; the sign (where explicitly indicated) was established from applied field Mössbauer spectra. [d] See comment made in the instruction about possible experimental complications for this species. [e] Abbreviations: pyS$_4$ = 2,6-bis(2-mercaptophenylthiomethyl)pyridine(2−), pyN$_4$ = 1,6-C$_5$H$_3$N[CMe-(CH$_2$NH$_2$)$_2$]$_2$.

Table 3. Spin Hamiltonian and Hyperfine Parameters of Complexes at 4.2 K

	1	**2**	**3**
S_t[a]	0	1/2	0
$A_x^{eff}/g_N\beta_N$ (^{57}Fe), T		−4.0(10)	
$A_y^{eff}/g_N\beta_N$ (^{57}Fe), T		−12.9(2)	
$A_z^{eff}/g_N\beta_N$ (^{57}Fe), T		+9.1(2)	
A_x(^{14}N), MHz		a, 3(9);[h] b, 54(6)[h]	
A_y(^{14}N), MHz		a, 75(3);[h] b, 63(3)[h]	
A_z(^{14}N), MHz		a, 30(6);[h] b, 54(6)[h]	
δ, mm s^{-1} [b]	0.02	0.28	0.41
ΔE_Q, mm s^{-1} [c]	+1.71	+0.86	+1.69
η[d]	0	0.4(2)	0.8(1)
g[h]		2.042(4), 2.022(2), 1.977(2) (a)	
		2.056(2), 2.012(3), 1.968(2) (b)	
Γ, mm s^{-1} [e]	0.33	0.50	0.31
α, β, deg[f]		10(10), 24(5)	

[a] Ground state. [b] Isomer shift. Typical errors of δ and ΔE_Q are ±0.02 mm s^{-1}. [c] Quadrupole splitting. [d] Asymmetry parameter of the EFG. [e] Line half-width. [f] Euler angles, rotation of the EFG with respect to **g** and **A** tensors. [g] g values of major component; for details of the EPR simulations, see Figure 11. [h] Values for EPR subspectra a and b; see Figure 9. Estimated uncertainties in the values are given in parentheses. [i] g values taken for Mössbauer simulations.

[Fe^{II}(CO)(pyS$_4$)] (δ = 0.19 mm s^{-1}), and [Fe^{II}(PR$_3$)(pyS$_4$)] (δ = 0.34 mm s^{-1}). All three complexes contain a low-spin ferrous ion, a common pyS$_4^{2-}$ ligand, and a sixth NO$^+$, CO, PR$_3$ π-acceptor ligand, respectively, of decreasing π-acceptor strength.[8]

Application of 1.5−7 T magnetic fields at liquid-helium temperatures for complexes **1**−**3** allowed the determination of the spin Hamiltonian and hyperfine parameters of these complexes at 4.2. They are given in Table 3. The spectrum shown in Figure 7(top) confirms the S_t = 0 ground state of **1** and establishes a large positive quadrupole splitting and a vanishing asymmetry parameter which reveals axial symmetry of the electric charge density of "pancake" appearance (V_{zz} > 0). This is consistent with the nearly axial symmetry of the FeNO moiety in **1**. Therefore, the main component V_{zz} of the electric field gradient (EFG) can be clearly assigned to the direction of the linear Fe−NO unit in **1**. The Mössbauer parameters of [Fe(NO)(pyS$_4$)]$^+$ are very similar. This shows that they are not very sensitive to the nature of the other ligands but are typical for the linear {Fe−NO}^{6} moiety.

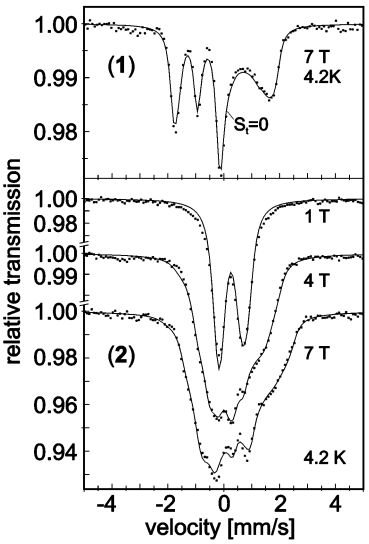

Figure 7. Top: Applied field (7 T) Mössbauer spectrum of **1** at 4.2 K. Bottom: Variable-field Mössbauer spectra of **2** at 4.2 K.

From variable-field magnetic Mössbauer spectra of **2** shown in Figure 7 (bottom) a positive sign for the quadrupole splitting is established and the S = 1/2 ground state is confirmed by the observed rather weak overall magnetic splitting. The hyperfine splitting parameters for both **2** and [Fe(NO)Cl(cyclam)]$^+$ (S_t = 1/2, $A_{iso}/g_N\beta_N$ = −2.6 and −5 T)[10] are small—in contrast to low-spin [Fe^{III}(N$_3$)(cyclam-ac)]$^+$ (S_t = 1/2; $\bar{A}/g_N\beta_N$ = (−41.2, 35.0, −6.3) T, $A_{iso}/g_N\beta_N$ = −4.2 T).[16] Note that the Mössbauer parameters for [Fe(NO)(pyS$_4$)]^0 (S_t = 1/2) are very similar to those of **2**.

Figure 8 shows zero- and applied-field Mössbauer spectra (4.2 K) of a frozen acetonitrile solution of one-electron reduced **2** after transfer to a Mössbauer sample holder which was successfully fitted with two subspectra a and b. The zero-field spectrum was also readily fitted by two subspectra a and b. Subspectrum b (66%) displays the same parameters as **2** and is therefore considered to correspond to the air reoxidation product **2** of the chemically generated reduced form **3**. Subspectrum a (34%) corresponds to a diamagnetic species (S_t = 0) with δ = 0.41 mm s^{-1}, ΔE_Q = +1.69 mm s^{-1}, and η = 0.798. It is assigned to [Fe(NO)(cyclam-ac)]^0, the {Fe−NO}^{8} (S_t = 0) species **3**.

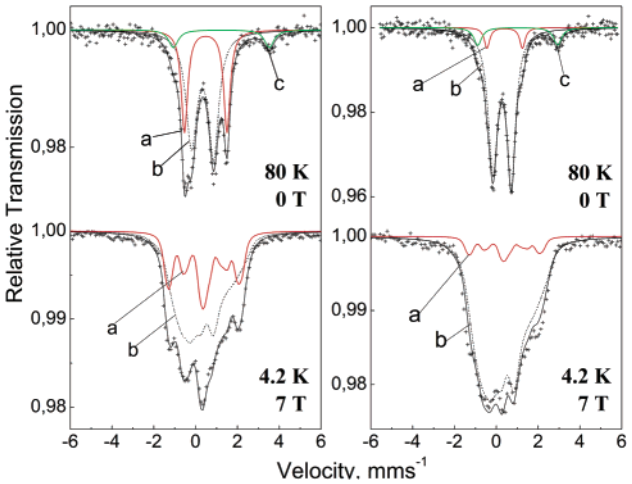

Figure 8. Applied-field Mössbauer spectrum of a one-electron reduced acetonitrile solution of **2** yielding **3** at 4.2 K. The spectrum was fitted by two subspectra of (a) **2** and (b) **3**. Parameters of **3** are given in Table 3.

5. EPR Spectroscopy. {FeNO}^{7} compounds are classical targets of EPR investigations due to the $S = {}^1/_2$ ground state and the rich *g*- and *A*-splittings of the spectra. Nevertheless, it proved to be difficult to obtain a unique and reproducible set of cw spectra from solutions of **2**, due to strong influences of solvent nature and sample concentrations on the spectral pattern. A major problem seems to be microheterogeneity of the solvated molecules, which partly yields very broad lines with frequency dependent widths. A reliable and reproducible data set was finally obtained from carefully degassed solutions of **2** in dried butyronitrile at low sample concentrations (≈0.1 mM), as shown in Figure 9A−C for three different microwave frequencies (Q-, X-, and S-band). As expected, the appearance of the low-frequency spectrum (Figure 9C, S-band) is determined by hyperfine splittings, whereas *g*-splittings dominate the pattern at high frequency (Figure 9A, Q-band). From the shape of the X-band spectrum (B) it seems to be clear that it is particularly the direction of the mid *g* value that shows significant hyperfine splittings due to interaction of the electronic spin with the ^{14}N nucleus ($I = 1$) of the NO ligand. However, a consistent fit of the three data sets with the appropriate Hamiltonian for $S = {}^1/_2$, $I = 1$, could not be obtained without the introduction of a second species, subspectra a and b in Figure 9, with intensity ratio a:b = 70:30. The presence of a distinct second subspectrum is most obvious from the resolved hyperfine pattern in the Q-band spectrum (A) at $g_{mid} = 2.012$, which is obscured by spectral crowding at the other frequencies. The parameters of the subspectra were obtained from simultaneous fits for the three EPR frequencies (Figure 9, Table 3).

6. Density Functional Calculations. In this section DFT calculations are reported with the goals to (a) interpret the spectroscopic properties of the investigated compounds, (b) develop a qualitatively appealing bonding pattern, (c) validate the accuracy of the calculations, and (d) obtain insight into the nature of the elusive {FeNO}^{8} species. In particular, we will address the question of formal oxidation state of the central iron and its relation to the spectroscopic IR, Mössbauer, and EPR observables. This is important since there are two sets of apparently conflicting data: from the point of view of the observed decreasing N−O stretching frequencies within the series ligand-centered reduction steps apparently prevail. However, the strong increase of the Mössbauer isomer shift along the series could be an indication for metal-centered redox chemistry. We will show that the present calculations lead to a unified and satisfactory explanation of all observations.

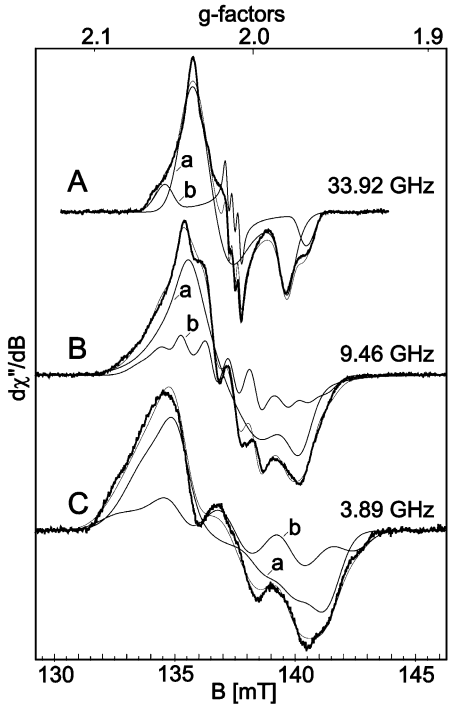

Figure 9. EPR spectra of **2** in frozen butyronitrile solution recorded at different microwave frequencies: (A) 33.9202 GHz, 0.2 mW power, 1 mT/100 kHz modulation, temperature 40 K; (B) 9.4565 GHz, 2 mW power, 0.5 mT/100 kHz modulation, temperature 10 K; (C) 3.8835 GHz, 2 mW power, 0.8 mT/100 kHz modulation, temperature 13 K. The thin lines are spin-Hamiltonian simulations for $S = 1/2$, $I = 1$, with parameters as given in Table 3 for subspectra a and b with integral intensity ratio 70:30. The line shapes were Gaussians, and the line widths were treated as independent fit parameters according to a *g*- and *A*-strain model (see Physical Measurements); we assume that they mainly parametrize unresolved sample heterogeneities. The line shape parameters are given in Table S11 of the Supporting Information.

6.A. Structures. The chemical identity of the {FeNO}^{6} (**1**) and {FeNO}^{7} (**2**) species was unambiguously established from X-ray structural analysis and comparison of spectra taken in solution and the solid state. However, the nature of the {FeNO}^{8} species is less clearly defined. We have therefore investigated the following possibilities (Chart 2): (a) reduction of the {FeNO}^{7} to the {FeNO}^{8} species (**3a**); (b) protonation of the {FeNO}^{8} species to give {FeHNO}^{8} with protonation either at the nitrogen (**3b**) or on the oxygen (**3c**); (c) transfer of a proton from a cyclam nitrogen to the NO to give a {FeHNO}^{8} core and an anionic amido ligand (**3d**).

Before discussing the optimized structure, it is interesting to study the O−N−Fe−N_{cyclam} dihedral angle in the {FeNO}^{7} and {FeNO}^{8} species which describes the rotation of the bent NO ligand over the FeN_4 plane. A rigidly scanned potential energy surface (PES; BP86/TZVP level) is shown in Figure 10. Interestingly, the {FeNO}^{8} PES features a significant barrier of ∼11 kcal/mol together with a double-minimum behavior. The two minima correspond to structures in which the N−O ligand is situated directly above the N−H bonds of the cyclam-acetate ligand (Figure 10). A weak hydrogen bonding of the type N−O···H−N_{cyclam} is therefore likely. By contrast, the PES obtained for the {FeNO}^{7} species is much flatter and shows a

Chart 2

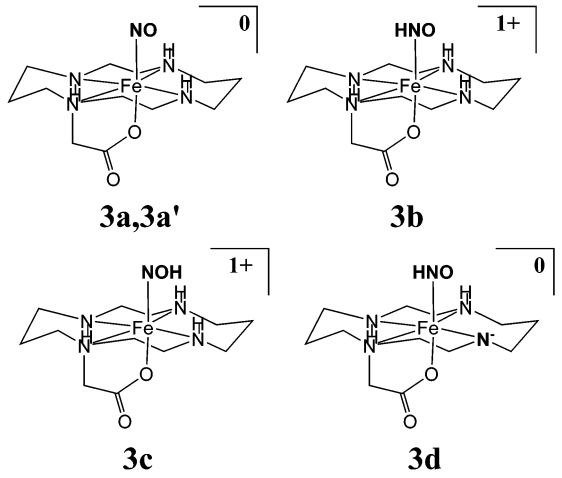

barrier of only <4 kcal/mol. The higher barrier for the {FeNO}^{8} form is rationalized by the longer N−O bond and particularly by the more acute Fe−NO bond angle both of which allow for a closer access of the NO oxygen to the cyclam N−H protons. The closest oxygen−hydrogen distance is 219.4 pm in {FeNO}^{8} and 233.6 pm in {FeNO}.^{7} Thus, there is a significant difference of ∼14 pm in this distance although the O−H distance is still fairly long for a hydrogen bond which in unconstrained systems typically is 170−180 pm. Nevertheless, the NO rotation appears to be significantly hindered in the {FeNO}^{8} form and the rotation should be 6−9 orders of magnitude slower than in the {FeNO}^{7} form. Since these calculations are rigid surface scans, the calculated barrier heights are certainly overestimated in both cases. Nevertheless, the calculations imply that the NO ligand in the {FeNO}^{7} form is more or less freely rotating while in the {FeNO}^{8} form the barrier is probably large enough to essentially lock the system into one minimum at room temperature. A similar conclusion was reached by Patchkovskii and Ziegler in their careful study of {FeNO}^{7} nitrosyl porphyrins.[45]

If the geometries of both species are relaxed starting from the two minima found for the {FeNO}^{8} species, two nearly isoenergetic minima (within 2 kcal/mol) were found for both the {FeNO}^{7} and {FeNO}^{8} species which will be labeled **2**, **2′** and **3a**, **3a′** in the following.

We are now in a position to compare selected calculated and experimental structure parameters in Table 4. In general, the calculations are in excellent agreement with the experimental structures. In particular the bond distances to the axial ligands are very well reproduced. In agreement with the experimental findings the {FeNO}^{6} unit is calculated to have an essentially linear Fe−N−O arrangement. This is also commonly observed in {FeNO}^{6} model hemes and hemoproteins.[46] In addition, both the Fe−N bond and the N−O bond are short. At the same level of theory a free NO^+ has a predicted bond length of 107 pm while a free NO has a bond length of 116 pm, in reasonable agreement with the experimental value of 115.1 pm.[47] Upon reduction to the {FeNO}^{7} form the FeN bond lengthens considerably by 6 pm, which is again in good agreement with the experimental observations. The crucial feature is the bending of the NO unit to an angle of ∼140°, which is well reproduced

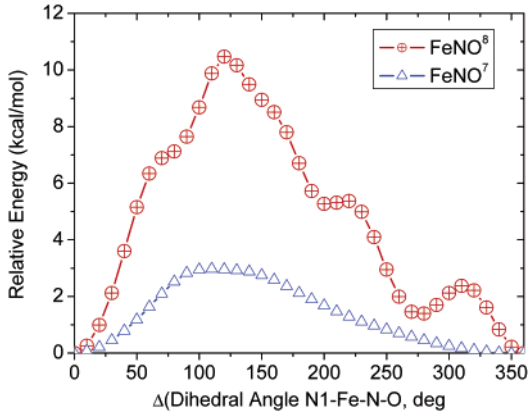

Figure 10. Rigidly scanned potential energy surface (BP86/TZVP) for the rotation of the NO ligand in the {FeNO}^{7} (**2**) and {FeNO}^{8} (**3**) species.

by the calculations. At the same time the N−O bond in the {FeNO}^{7} form is considerably lengthened to ∼120 pm and the trans-effect of the NO on the axial carboxylate appears to be reduced as is evident in a reduced Fe−O bond length. A further reduction step to {FeNO}^{8} unit leads only to a slight lengthening of the Fe−N bond to about ∼175 pm but a considerable further lengthening of the N−O bond to 126 pm (free NO^- in the gas phase has an estimated bond length of ∼125 pm[48] in good agreement with the calculated value of 128 pm). The Fe−O distance lengthens by ∼14 pm in this step which, on the basis of experience with similar complexes, is probably an overestimate. The FeNO bond angle is predicted to be more acute than in the {FeNO}^{7} form and almost reaches 120°, which is consistent with sp^2 hybridization at N. The protonated species {FeHNO}^{8} (**3b**) has geometrical parameters similar to the unprotonated form except for the Fe−O bond which shrinks again to about 198 pm and a slightly less acute Fe−NO bond angle of ∼132 pm. The O-protonated species (**3c**) features a much longer N−O bond of ∼138 pm and a short Fe−N bond of 171 pm.

6.B. Energetics. For the {FeNO}^{8} level the "internally protonated species" (**3d**) is calculated to be 19.3 kcal/mol less stable than the {FeNO}^{8} form (**3a**) and is therefore ruled out. For the protonated species **3b**,**c** the O-protonated form (**3c**) is 22.9 kcal/mol higher in energy than the N-protonated species (**3b**) and is therefore also ruled out.[49] This value is in good agreement with our earlier, less rigorous, estimate in the context of the reaction mechanism of CCNIR.[15] These results leave us with **3a**,**3a′** and **3b** as the only plausible candidates for the observed {FeNO}^{8} species. However, below we will show that only the {FeNO}^{8} (**3a**) and not the {FeHNO}^{8} (**3b**) species is consistent with the observed spectroscopic properties of the reduced species.[50]

(45) Patchkovskii, S.; Ziegler, T. *Inorg. Chem.* **2000**, *39*, 5354−5364.
(46) Wyllie, G. R. A.; Scheidt, W. R. *Chem. Rev.* **2002**, *102*, 1067−1089.
(47) Brown, J. M.; Cole, A. R. H.; Honey, F. R. *Mol. Phys.* **1972**, *23*, 287.
(48) Siegel, M. W.; Celotta, R. J.; Hall, J. L.; Levine, J.; Bennett, R. A. *Phys. Rev. A* **1972**, *6*, 607.
(49) In addition to the structures described above, some alternatives were also considered in an earlier stage of the project. Structures with side-on bound NO could be located as energy minima for the {FeNO}^{6} and {FeNO}^{7} forms. However, in the {FeNO}^{6} case this structure is predicted to be ∼35 kcal/mol less stable than the end-on bound structure and in the {FeNO}^{7} case the energy difference amounts to ∼27 kcal/mol. For {FeNO}^{8} no stable side-on structure was found. Since the side-on structures are much higher in energy and are also inconsistent with the experimental observations they were not further investigated. In addition, we have looked for a broken symmetry solution of the {FeNO}^{8} form which corresponds to an electronic structure description of Fe(III) (low spin, $S_{Fe} = 1/2$) antiferromagnetically coupled to $NO^\bullet$ ($S_{NO} = 1/2$). Whether starting from an end-on or a side-on structure, the calculations converged back to a closed-shell species.

Table 4. Selected Geometrical Parameters (in pm and deg) Obtained from BP86/TZVP Calculations (Experimental Values When Available in Parentheses)

	Fe–N	N–O	∠(Fe–N–O)	Fe–O–C=O	Fe–N_{av} [a]
{FeNO}^{6} (**1**)	166.2 (166.3)	115.9 (113.3)	179.1 (175.6)	186.4 (188.3)	206.6 (200.9)
{FeNO}^{7} (**2**)	172.3 (172.2)	120.4 (116.7)[b]	140.6 (148.7)[b]	198.1 (201.2)	205.2 (202.5)
{FeNO}^{7} (**2′**)	172.6	120.6	138.8	198.2	205.1
{FeNO}^{8} (**3a**)	175.2	126.1	122.4	212.7	204.8
{FeNO}^{8} (**3a′**)	175.6	127.0	118.9	211.3	204.2
{FeNO}^{8} (**3d**)	177.6	127.4	133.0	202.9	203.1
{FeHNO}^{8} (**3b**)	178.0	126.8	126.3	199.4	203.8
{FeNOH}^{8} (**3c**)	171.0	138.1	123.6	198.5	205.3

[a] Average distance from the iron to the four cyclam nitrogens. [b] Two species are refined in the experimental structure. The second species has an Fe−N−O angle of 146.1° and a N−O distance of 113.0 pm.

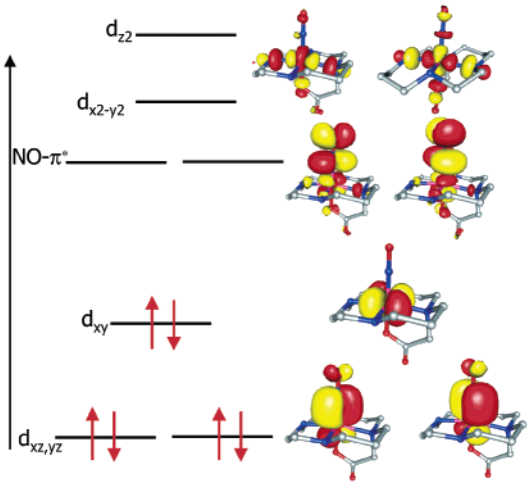

Figure 11. Frontier molecular orbitals of {FeNO}^{6} as calculated by the spin-restricted B3LYP method. The occupied orbitals were localized with the Pipek− Mezey algorithm.

The precise binding energies of the NO ligand in the different redox states in solution is difficult to estimate with sufficient accuracy. However, we have simulated an aqeous solution by the COSMO approximation and included zero-point and thermal effects in the calculations. The highest binding energy is calculated for **2** which is stable toward dissociation into the five-coordinated [Fe(cyclam-acetate)]$^+$ and NO by ∼51 kcal/mol, whereas **1** and **3a** have binding energies of less than 10 kcal/mol. This result confirms {FeNO}^{7} as the thermodynamic sink of iron−nitrosyl chemistry as evidenced by the much larger number of known {FeNO}^{7} complexes compared to {FeNO}^{6} or {FeNO}^{8} species.

6.C. Bonding. For the purpose of analysis it is convenient to transform the occupied Kohn−Sham orbitals to localized MOs (LMOs) to allow the interpretation of the calculational results in familiar chemical terms. The calculated LMOs for the {FeNO}^{6} species (**1**) are shown in Figure 11. Three doubly occupied orbitals of mainly iron character can be identified. This set involves an essentially nonbonding d_{xy} orbital and a strongly π-bonding set of d_{xz} and d_{yz} orbitals. The latter set is almost degenerate due to the essentially C_{4v} symmetry of the complex core. The strongly π-bonding set consists of ∼70% iron and ∼30% NO-π^* character which is consistent with early MO calculations on {FeNO}^{6} species.[1] The lowest unoccupied orbitals (the virtual orbitals were *not* localized) are mainly NO-π^* in character. However, they have ∼30% Fe character and are strongly π-antibonding. Next in energy are the e_g-derived iron orbitals ($d_{x^2-y^2}$ and d_{z^2}), both of which are σ-antibonding with the ligands. This orbital structure strongly implies the description of the electronic structure of {FeNO}^{6} in terms of a low-spin central Fe(II) ion bound to a NO^+ ligand. However, NO^+ is an extremely strong π-acceptor. Therefore, the occupied iron t_{2g} derived orbitals are *bonding* and contain a large amount of NO-π^* character. This NO-π^* character signifies a large amount of charge transfer from the iron to the NO^+ ligand. At the same time this very strong back-bonding interaction strengthens the Fe−NO bond and weakens the N−O bond. Consequently, the observed (and calculated) Fe−N bond is very short (<170 pm) and the N−O bond is significantly longer than expected for a free NO^+. This means that due to the back-bonding some of the triple-bond character of the NO^+ is lost. Still the description of low-spin Fe(II) bound to NO^+ appears to be fairly unambiguous from the calculations and we will show below that it is also consistent with all spectroscopic data.

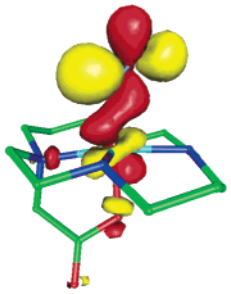

Figure 12. Singly occupied MO in the {FeNO}^{7} species. Shown is the singly occupied natural orbital from a spin-unrestricted B3LYP Kohn−Sham calculation.

The analogous analysis has also been performed for the {FeNO}^{7} (**2**) and {FeNO}^{8} (**3a**) cases. On the basis of the MO scheme for **1** (Figure 11), the first additional electron enters a NO-π^*-based MO which is essentially degenerate. Thus, a Jahn−Teller distortion is expected and the bending of the Fe−NO unit can be interpreted as arising from such a distortion.[1,7,9] The result is that the two NO-π^* orbital are split into a σ-antibonding (with respect to the iron) π^*_σ orbital and a higher-lying π-antibonding (with respect to the iron) π^*_v orbital. The unpaired electron therefore resides in the π^*_σ orbital. This is also observed in the spin-unrestricted Kohn−Sham calculations at either the BP86 or B3LYP levels. The SOMO (shown as the singly occupied natural orbital in Figure 12) has ∼25% iron character due to bond formation between π^*_σ and the iron t_{2g} (d_{xz}) and e_g (d_{z^2}) orbitals. The interaction with the d_{z^2}

(50) Unfortunately, precise pK_a values in solution are difficult to calculate (our attempts using isodesmic reactions indicated a strong dependence of the results on proton donor) such that one cannot reliably estimate the likeliness of protonation from theory alone.

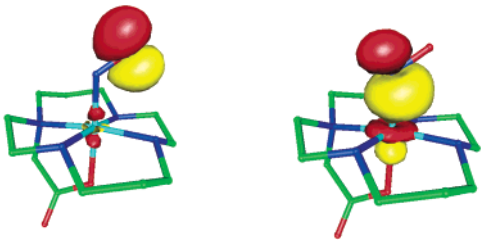

Figure 13. Splitting of the N−O π-bond leading to an oxygen-centered lone pair (left) and a nitrogen-centered lone pair (right) in the $\{FeNO\}^8$ species **3a**. The oxygen-based lone pair is oriented for hydrogen bonding to the cyclam ligand, and the nitrogen-based lone pair is bonding to the iron.

component is seen to be bonding which is due to the fact that the d_{z^2} orbital is higher in energy than the NO-π^* orbitals. The antibonding character in the SOMO derives from the t_{2g} contributions to this MO.

Lower in energy one can find three doubly occupied orbitals that are mainly iron in character and that are analogous to the occupied orbitals of **1**. On the basis of these findings, we conclude that the electronic structure of the $\{FeNO\}^7$ form (**2**) is best described as a low-spin Fe(II) with a coordinated $NO^\bullet$ radical. Since the reduction step has mainly occurred at the ligand, it becomes much less electrophilic than the coordinated NO^+ in the $\{FeNO\}^6$ species, and consequently, the back-bonding interaction between iron and $NO^\bullet$ is much weaker than in the $\{FeNO\}^6$ case. The calculations indicate that the back-bonding via the π-pathway is reasonably similar to the $\{FeNO\}^6$ case (~28% NO character) while via the mixed π/σ pathway provided by the π^*_σ orbital ~20% NO character is mixed into the iron orbitals. This reduced π-back-donation nicely rationalizes the increase in the Fe−N bond length from ~166 pm to ~172 pm. At the same time the NO bond is considerably weakened due to the addition of an extra electron into a π^* orbital, which is strongly N−O antibonding and explains the lengthening of this bond.

In the $\{FeNO\}^8$ case (**3a**) analoguous considerations apply. Again, three doubly occupied orbitals are found that are mainly iron in character, and consequently, the valence state of the iron is still low-spin Fe(II). In the calculations, the additional electron pairs up with the unpaired electron in the $\{FeNO\}^7$ SOMO to give a closed-shell species. Since the $\{FeNO\}^7$ SOMO is essentially localized on the NO ligand, the best description in terms of limiting valence structures is therefore low-spin Fe(II) bound to NO^- ($S_{NO} = 0$). The $S_t = 0$ spin state, which is also observed experimentally, is favored by the strong tilting of the Fe−NO bond which leads to a significant splitting of the π^*_σ and π^*_v orbitals such that it becomes energetically more favorable to doubly occupy π^*_σ instead of forming a state with $S_{NO} = 1$ through single occupation of π^*_σ and π^*_v as it would occur for a free $^3NO^-$ which is isoelectronic with $^3O_2$. In fact, the lowest triplet state of **3a** is predicted to be higher in energy by 9.6 kcal/mol at the B3LYP level.

The complete occupation of one of the NO π^* orbitals in **3a** leads to splitting of this bond and leaves a double bond in the NO^- ligand and two lone pairs on the nitrogen and oxygen, respectively. As shown in Figure 13 (right), the lone pair on the nitrogen is involved in a σ-bond with the formally uncoccupied d_{z^2} orbital in the iron. This is the rationale for the observation that the iron−nitrogen bond length stays short in **3a** (Table 4). On the other hand, the oxygen lone pair is oriented in a way suitable for hydrogen bonding with the cyclam N−H group (Figure 13). This is one of the rationales for the significant barrier of rotation and may also help to explain that the elusive $\{FeNO\}^8$ species can form at all in our system.

Table 5. Natural Charges and Populations Obtained from the Analysis of the B3LYP Densities

	Fe	3d/4s/4p	NO/H
$\{FeNO\}^6$ (**1**)	0.965	6.75/0.27/0.01	0.171
$\{FeNO\}^7$ (**2**)	1.005	6.73/0.25/0.01	−0.230
$\{FeNO\}^7$ (**2′**)	1.004	6.73/0.25/0.01	−0.226
$\{FeNO\}^8$ (**3a**)	0.882	6.86/0.23/0.02	−0.672
$\{FeNO\}^8$ (**3a′**)	0.891	6.86/0.23/0.02	−0.690
$\{FeNO\}^8$ (**3d**)	0.999	6.76/0.24/0.02	−0.613/0.219
$\{FeHNO\}^8$ (**3b**)	1.010	6.74/0.24/0.01	−0.555/0.324
$\{FeNOH\}^8$ (**3c**)	1.005	6.74/0.24/0.01	−0.639/0.428

The bonding in the $\{FeHNO\}^8$ species (**3b**) can also be satisfactorily explained from the calculations (Figure S2). In the localized MOs one can find three orbitals of mainly iron character one of which (labels d_{xz} in Figure S2) is involved in a strong π-back-bonding interaction with the HNO ligand. The lowest unoccupied MOs feature an empty mainly HNO-π^* orbital and the two metal-based empty e_g like MOs. Thus, the description of this species also features a low-spin Fe(II) bound to a neutral HNO ligand. However, compared to the unprotonated species (**3a**), the back-bonding between iron and HNO is stronger, since protonation lowers the energy of all NO orbitals and therefore allows for a more efficient interaction between the formally empty NO-π^* and iron-based t_{2g} orbitals. This is also seen in the iron contribution to the "d_{xz}" orbital which is 73% in **3a** but only 65% in **3b**. Compared to the $\{FeNO\}^6$ species (**1**) the N−O bond order is reduced to a double bond and the oxygen and nitrogen each feature two lone pair orbitals. The nitrogen lone pairs are involved in bonding to the iron and the proton, respectively, and therefore, only one π^* orbital is available for back-bonding in **3a**,**b** compared to two in **1**. These results are in agreement with other calculations on coordinate HNO species.[15,33,34]

The notion of essentially ligand-centered reduction steps in the series $\{FeNO\}^6$, $\{FeNO\}^7$, and $\{FeNO\}^8$ is also consistent with the results of the natural population analysis (NPA) in Table 5. The charge on the central iron ion changes by less than 0.1 e^- in the series, and in particular, the d-electron population stays almost invariant. The number ~6.7 3d-electrons is consistent with the interpretation of a closed-shell d^6 electron configuration at the central iron with the extra electron density in the 3d-orbitals arising from charge donation of the ligands into the formally empty, σ-antibonding iron e_g orbitals. By contrast, the natural charge on the NO unit is undergoing fairly large changes in the series and becomes ~0.4 electrons more negative in each reduction step. This is probably as close to a full ligand-centered reduction as one will ever obtain since changes of atomic partial charges in a molecule of the order of a full unit of charge are unrealistic on the basis of electroneutrality considerations.

We therefore conclude from the analysis of the Kohn−Sham orbitals and the natural population analysis that, in agreement with other recent theoretical results,[13] the reduction steps are essentially ligand centered.

6.D. Spectroscopy. 6.D.1. IR Spectra. Of particular interest in the vibrational analysis is the NO-stretching frequency (ν_{NO}),

Table 6. Calculated Vibrational Frequencies and Isotope Shifts (cm^{-1}) Together with Quasi-Diatomic Force Constants (mdyn/Å) (BP86/TZVP Level)

	ν_{NO}	$\Delta(^{15}N^{18}O)$	$\nu_{C=O}$	f_{Fe-N}	f_{N-O}
{FeNO}^{6} (**1**)	1871	−80	1758	3.93	13.97
{FeNO}^{7} (**2**)	1600	−67	1706	2.61	10.43
{FeNO}^{7} (**2′**)	1591	−67	1706	2.52	10.32
{FeNO}^{8} (**3a**)	1331	−69	1659	2.37	7.19
{FeNO}^{8} (**3a′**)	1312/1281	−47	1662	2.26	6.69
{FeNO}^{8} (**3d**)	1309/1298	−56	1672	2.26	6.51
{FeHNO}^{8} (**3b**)	1351	−73	1710	2.26	6.81
{FeNOH}^{8} (**3c**)	834	−33	1706	2.78	2.14

which is a marker vibration for the NO bond (section 1). The calculated[51] vibrational frequencies for the NO stretching vibration are collected in Table 6 (analogous interpretations apply for the isomers **2**, **2′**, **3a**, and **3a′**). For the {FeNO}^{6} (**1**) and {FeNO}^{7} (**2**) species the agreement of the calculated and observed vibrational frequencies is good and lends support to the electronic structure descriptions obtained for these species. In both cases the ν_{NO} stretches are well-isolated modes, which is consistent with the good agreement between calculated and observed isotope shifts. The downshift of the N−O stretching vibration is associated with a softening and lengthening of the N−O bond due to the loss of N−O triple bond character. For the {FeNO}^{8} species the N−O stretching vibration is so low in energy that it falls into a rather crowded region of the IR spectrum. The mode with the largest N−O stretching character is predicted at 1274 cm^{-1}, in good agreement with the experimentally determined 1271 cm^{-1}. Upon $^{15}N^{18}O$ substitution in silico, the mode shifts to 1217 cm^{-1}, which is smaller than the experimentally determined 1228 cm^{-1} but in good agreement with the simple harmonic model. The predicted isotope shifts for **1** and **2** of −80 and −67 cm^{-1} are in excellent agreement with the experimental values of −81 and −62 cm^{-1}, respectively, and indicate a limited amount of mechanical coupling in these ν_{NO} modes. For the hypothetical {FeHNO}^{8} species the N−O stretch is calculated at 1351 cm^{-1}, which is far from the experimentally observed number for the reduced species. The {FeNOH}^{8} species has an N−O bond that is essentially reduced to a single bond and consequently displays a ν_{NO} frequency of only 834 cm^{-1}, which is in the range of frequencies found for coordinated hydroxylamine ligands.[52] Thus, these results also strongly favor the {FeNO}^{8} (**3a**) description over {FeHNO}^{8} (**3b**) or {FeNOH}^{8} (**3c**).

The trends in the C═O stretching vibrations are also well reproduced by the calculations and confirm the status of this vibrational mode as a good marker for the electronic and geometric changes that occur trans to the carboxylate group. The trend in the frequency of the C═O mode is rationalized through a loss of double bond character by going from the {FeNO}^{6} to the {FeNO}^{8} form. The origin of this effect is the reduced covalency of the Fe−O bond along the series due to the loss of Fe−NO back-bonding. This reduces the charge donation of the COO^- group to the central iron and consequently leads to more charge delocalization into the C═O π^* antibonding orbital, which is accompanied by a decrease in the C═O stretching frequency. This also explains the lengthening of the Fe−O bond upon reduction. The C−O stretching vibration is difficult to determine unambiguously from the calculations due to spectral crowding in the region 1200−1400 cm^{-1} and was therefore not analyzed.

The trends in the vibrational frequencies are also nicely reflected in the calculated quasi-diatomic force constants (neglecting mechanical coupling to other modes) for the Fe−NO and N−O bonds collected in Table 6. It is seen that the stiffness of the Fe−NO bond decreases slightly along the series while the N−O bond becomes softer by ∼ 3 mdyn/Å per redox step. The decrease in back-bonding along the series can be estimated by comparing the f_{N-O} to the values obtained for the free NO^+, NO, and NO^- ligands. The values in Table 6 correspond to 44% (**1** versus NO^+), 33% (**2** versus NO), and 11% (**3a** versus NO^-) decrease thus showing that the weakening of the NO bond by back-bonding strongly decreases along the series.

It is also interesting to compare the calculated N−O stretching frequencies with the data obtained for a series of small $H_xN_yO_z$ species in Figure S3. A nearly linear correlation is found between the N−O stretching frequency and the N−O bond length which holds for different total charges, spin states, and protonation levels. On the basis of these data, the free NO^+ ligand in the gas phase should have a stretching frequency in the range ∼2300 cm^{-1} (Westcott and Enemark give this value as ∼2200 cm^{-1}) while free NO has a predicted ν_{NO} of 1881 cm^{-1} (experimental 1904 cm^{-1}).[47] For free NO^- the calculated frequency is 1357 cm^{-1} (experimental 1363 cm^{-1}).[53] Thus, the values of 1903 cm^{-1} found in the {FeNO}^{6} species, 1611 cm^{-1} in the {FeNO}^{7} species, and 1273 in the {FeNO}^{8} species correspond to ∼20%, ∼15%, and ∼7% reduction of ν_{NO} relative to the uncoordinated ligands, which nicely parallels the trend obtained for the mechanical coupling corrected force constants. This is interpreted as an effect of the iron to NO back-donation which transfers electron density into the NO-π^* orbitals and therefore weakens the NO bond. The numbers are also consistent with the idea that the back-bonding ability of the NO ligand strongly decreases along the series NO^+, NO, NO^- in which the NO ligand changes its character from a strong electrophile to a potent nucleophile. In the {FeHNO}^{8} species (**3b**), ν_{NO} is reduced by ∼15% compared to free HNO, which is consistent with stronger π-back-bonding in **3b** compared to the unprotonated species **3a**.

6.D.2. Mössbauer Spectra. The Mössbauer isomer shift (IS), δ, and the quadrupole splitting (QS) parameter, ΔE_Q, were calculated with the B3LYP DFT method for all models according to the procedures given in ref 36 (Table 7). The calculations lead to very good (IS; maximum error 0.05 mm/s) and reasonable (QS) agreement with experiment. Again, the {FeHNO}^{8} species (**3b**) leads to calculated Mössbauer parameters which are not in agreement with the experimental data while the {FeNO}^{8} formulation (**3a**) does.

(51) The harmonic frequencies calculated with the BP functional are generally known to compare favorably with experimentally measured fundamental frequencies. This is based on a partial cancellation of errors since the experimental frequencies would have to be corrected for anharmonicities to be strictly comparable to the theoretical numbers.[29] However, the anharmonicity corrections are unknown for molecules of the size studied in this work. We therefore directly compare the calculated frequencies with the experimental vibrational frequencies as observed by IR spectroscopy. The experimentally observed shifts within the series of FeNO complexes and in the isotopic labeling experiments are sufficiently large to be unambiguously correlated with the theoretical numbers.

(52) Wieghardt, K. *Adv. Inorg. Bioinorg. Mech.* **1984**, *3*, 213−274.

(53) Tronc, M.; Huetz, A.; Landau, M.; Pichou, F.; Reinhardt, J. *J. Phys. B* **1975**, *8*, 1160.

Table 7. Calculated Mössbauer Parameters at the B3LYP Level

	δ, mm/s	ΔE_Q, mm/s	η
{FeNO}^{6} (**1**)	0.053	1.101	0.098
{FeNO}^{7} (**2**)	0.276	−0.756	0.826
{FeNO}^{7} (**2′**)	0.275	−0.756	0.826
{FeNO}^{8} (**3a**)	0.424	1.556	0.731
{FeNO}^{8} (**3a′**)	0.407	1.615	0.488
{FeNO}^{8} (**3d**)	0.209	−1.740	0.298
{FeHNO}^{8} (**3b**)	0.251	1.344	0.910
{FeNOH}^{8} (**3c**)	0.178	1.879	0.424

The sensitivity of the Mössbauer isomer shift has been the strongest point in favor of metal-centered oxidation/reduction steps in the series {FeNO}$^{6-8}$.[10] The shift of ∼0.25 mm/s per oxidation state is consistent with a full one-electron oxidation or reduction of the metal ion. However, the good agreement of the present calculations with the experimental IS's led to the conclusion that an alternative interpretation is to be preferred. Importantly, the IS's correlate strongly with the back-bonding ability of the NO ligand. This correlation has been established in a recent study that has compared NO and NO^+ with CO, PR_3, and SR_2 ligands.[8] The results show that changes on the order of 0.5 mm/s are possible in FeL_5X depending on the back-bonding ability of the axial ligand X. Thus, the stronger the back-bonding, the smaller the IS. On the basis of this notion, NO^+ is by far the most strongly back-bonding ligand available, followed by NO (and CO), whereas NO^- has the smallest back-bonding ability.

The rationale for the correlation has been provided recently.[36] According to this interpretation the 3d-population as well as the direct valence 4s contributions are the strongest contributors to the *variations* in the IS along a series of iron-containing complexes. Thus, the more strongly back-bonding the axial ligands are, the more electron density is preferentially taken out of the iron 3d shell, the 3d shielding decreases, and the electron density at the iron nucleus increases. At the same time the metal−ligand bond length shrinks which leads to a distortion of the valence 4s contribution to the bonding orbitals to contract which further increases the electron density at the nucleus. In the present case it therefore also becomes understandable that the {FeHNO}^{8} species (**3b**) shows a strong decrease in the Mössbauer IS relative to the {FeNO}^{8} species (**3a**). The added proton strongly decreases the nucleophilicity of the bound NO^- and allows for more efficient transfer of electron density from the iron to the HNO which, in turn, will increase the electron density at the iron nucleus and decrease the IS.

The general trend in the quadrupole splitting, QS, observed experimentally is reproduced by our calculations (Table 7): $|\Delta E_q|$ decreases from **1** to **2** and increases from **2** to **3a**. The asymmetry parameter η is small for **1** and large for **2** and **3a**. These results are difficult to interpret since our interpretation invokes a low-spin Fe(II) central ion with a closed-shell, low-spin d^6 configuration for which there is no direct ligand field contribution to the EFG. Therefore, some shortcomings also warrant analysis. Thus, the QS is underestimated by our calculations for **1** and of the wrong sign for **2**. Since the calculated η for **2** is close to 0.9, the latter failure becomes less severe as a slight change in the individual components of the tensor would change its sign to be consistent with experiment. In fact, the magnitudes of the smallest and largest eigenvalue of the field gradient tensor differ by less than 0.04 au^{-3}, which is within the error limits of the theoretical methodology. Thus, the correct order of magnitude of the absolute values of ΔE_q is the more significant result for **2**. Below we examine what are the causes of the variations in the Mössbauer parameters along the series.

Table 8. Breakdown of Individual Contributions to the Electric Field Gradient at the Iron Center (in au^{-3}) for Complexes **1**−**3** As Predicted by the B3LYP Method

	{FeNO}^{6} (**1**)	{FeNO}^{7} (**2**)	{FeNO}^{8} (**3a**)	{FeHNO}^{8} (**3b**)
local	0.500	−0.640	1.001	0.813
lattice	0.026	0.003	0.005	−0.004
bond	0.108	0.219	−0.097	−0.075
three-center	0.044	−0.003	−0.025	−0.002
tot.	0.677	−0.421	0.883	0.733

The largest element of the field gradient tensor, $q \equiv V_{zz}$, is examined in Table 8 (z is defined here as the direction of the largest EFG principal component). In MO theory the value of q is simply given by the expectation value of the field gradient operator over the ground-state wave function and may be decomposed as in eq 3:[54]

$$q = q_{\text{local}} + q_{\text{lattice}} + q_{\text{bond}} + q_{3-\text{center}} \tag{3}$$

In this equation q_{local} is the local contribution of the iron orbitals to the field gradient. The "lattice" contributions, q_{lattice}, are often assumed to be the next largest part which arise from the net charges of the surrounding atoms. The bond contribution, q_{bond}, is not usually discussed but arises from the electron density in the bonds formed between the iron ion and the ligands. Finally, the three-center contribution, $q_{3-\text{center}}$, is a genuine nonlocal contribution and arises from the electron density in bonds that do not involve the Mössbauer absorber. It is usually neglected.

From the individual contributions summarized in Table 8 it is evident that the largest contribution to the EFG comes, as expected, from the local contributions at the iron site. Somewhat surprisingly, the lattice contribution is small and contributes essentially nothing to the variation across the series. The three-center contribution is small but changes across the series such that a maximum of ∼0.1 au^{-3} can be attributed to this term. The two-center bond contribution is, in fact, the second largest contribution and contributes up to ∼0.2 au^{-3} to the variation across the series.

The value of q_{local} may be further decomposed as in eq 4:

$$q_{\text{local}} = q_{\text{core}} + q_{t_{2g}} + q_{\text{cov}} \tag{4}$$

Here q_{core} comes from small aspherical distortions of the core-level 2p and especially 3p orbitals, $q_{t_{2g}}$ arises from anisotropy in the iron-based t_{2g} orbitals, and q_{cov} is due to the iron character in the ligand based orbitals. In ligand field theory one may write

$$q_{t_{2g}} \approx 2(^4/_7\alpha_{xy}{}^2 - {}^2/_7\alpha_{xz}{}^2 - {}^2/_7\alpha_{yz}{}^2)\langle r^{-3}\rangle_{\text{Fe}_{3d}} \tag{5}$$

where $\alpha_i{}^2$ is the fractional iron character in the ith iron t_{2g}-based orbital. Clearly, as $\alpha_{xy}{}^2 \neq \alpha_{xz}{}^2, \alpha_{yz}{}^2$ nonzero contributions proportional to the anisotropic π-covalency at the iron site will arise that correlate with the strength of the back-bonding. If we restrict our attention to the iron atom itself and its nearest neighbors, one can recover ≥80% of the value of q_{local} by

(54) Gütlich, P.; Link, R.; Trautwein, A. *Mössbauer Spectroscopy and Transition Metal Chemistry*; Springer: Heidelberg, New York, 1978.

Table 9. Further Breakdown of the Local Contributions to the Electric Field Gradient at the Iron Center for Complexes as **1**−**3** As Predicted by the B3LYP Method (in au^{-3})

	{FeNO}^{6} (**1**)	{FeNO}^{7} (**2**)	{FeNO}^{8} (**3a**)	{FeHNO}^{8} (**3b**)
q_{core}	−0.762	−0.0789	0.271	0.128
$q_{t_{2g}}$	2.120	−0.947	0.088	0.370
q_{cov}	−0.952	0.133	0.559	0.296
q'_{local} [a]	0.406	−0.893	0.917	0.798

[a] q'_{local} is restricted to the contributions of iron orbitals and orbitals localized on the nearest neighbors.

looking at individual contributions from Pipek−Mezey-localized orbitals (Table 9). It is evident that the $q_{t_{2g}}$ is dominant in the case of the {FeNO}^{6} species, **1**, which is due to the exceptionally strong back-bonding between Fe(II) and NO$^+$ which leads to large anisotropic covalency contributions ($\alpha_{xy}^2 \approx 1$; $\alpha_{xz,yz}^2 \approx 0.65$). For **2**, the back-bonding is reduced and the anisotropic covalency contribution becomes smaller in magnitude. However, it is still significant since there is a partial hole character in the d_{xz}-based MO. For **3a**, finally the back-bonding and therefore also $q_{t_{2g}}$ becomes small while, consistent with the discussion of the vibrational data and the IS's (vide supra), the value increases again for the protonated species **3b**. The final value of q'_{local} for **1** nevertheless arises from a partial cancellation of three large terms which enter with variable sign. In particular, the value of q_{cov} caused by the strong covalency of the axial ligands is large as is the core polarization. Given this delicate balance of opposing contributions the calculated value, despite its large error of ∼0.6 mm/s, seems to be acceptable. The value of q_{cov} becomes much smaller for **2** and **3b**, which carry essentially neutral axial (H)NO ligands, while it increases again for **3a**, which essentially coordinates NO$^-$. The value of core polarization is rather large but, unfortunately, does not lend itself to a simple interpretation.

Finally, the calculated field gradient tensor orientation is shown in Figure 14. In **1** the largest component of the field gradient tensor is, as expected, oriented almost exactly along the Fe−NO bond. For **2** and **3a** a reorientation occurs and the largest component is now oriented perpendicular to the Fe−N−O plane due to the bending off the N−O ligand and the associated changes in the anisotropic covalency contributions. Note that for **2** the negative EFG component along the projection of the N−O bond in the *x*,*y* plane is slightly larger in magnitude than the positive component perpendicular to the Fe−N−O plane. This slight error in the calculation leads to the wrong sign of the predicted QS. However, we believe that the largest EFG component has the same direction in both **2** and **3a**.

In conclusion, the Mössbauer IS's along the series {FeNO}$^{6-8}$ do *not* reflect oxidation state changes at the iron site but the different degrees of back-bonding with the changing chemical character of the NO ligand. The calculated field gradient tensors show the correct trend with respect to experiment and has been analyzed in detail.

6.D.3. EPR Spectra. On the basis of the electronic structure description given above, the EPR spectra of **2** can be readily interpreted. The large spin density on the NO ligand gives rise to a large ^{14}N-nitrogen hyperfine coupling seen experimentally and a small internal magnetic field established by the Mössbauer experiments. Since the spin density is mainly located on the ligand, the *g*-shifts are relatively small, which reflects the small spin−orbit coupling constants of N (∼75 cm^{-1}) and O (∼150 cm^{-1}) compared to Fe (∼400 cm^{-1}). However, a more detailed interpretation of the **g**-tensor is more subtle (vide infra and Supporting Information).

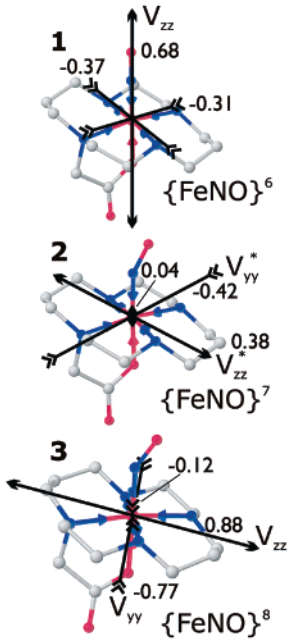

Figure 14. Calculated orientation of the EFG tensor in the molecular coordinate system (B3LYP method). Outward pointing arrows represent positive principal values, and inward pointing arrows negative principal values of the EFG tensor. Magntidues are given in au^{-3}. The principal component with the largest magnitude is labeled V_{zz} except for **2** where we have relabeled the principal axes to obtain an EFG sign consistent with experiment.

Table 10. Predicted **g**-Tensor and Nitrogen Hyperfine Tensor for the {FeNO}^{7} Species **2** from B3LYP DFT Calculations (Values Calculated for **2′** in Parentheses)

	min	mid	max
g-tensor	1.940 (1.943)	1.997 (1.996)	2.017 (2.023)
$A(^{14}NO)$, MHz	+11.4 (+13.4)	+25.9 (+19.9)	+86.2 (+86.7)
A_{iso}, MHz		+36.5 (40.0)	
$A(^{57}Fe)$, MHz	−9.6 (−9.6)	2.3 (−0.1)	29.5 (29.7)
$A(^{57}Fe)/g_N\beta_N$, T	−7.0 (−7.0)	1.7 (−0.07)	21.4 (21.6)
A_{iso}, MHz		+8.3 (+7.0)	
$A_{iso}/g_N\beta_N$, T		+6.0 (+5.1)	

The calculated magnetic coupling parameters are presented in Table 10. Due to the complicated superposition of two species, a definitive conclusion about their accuracy appears to be difficult to draw. However, the calculations show the correct pattern of a rhombic **g**-tensor with the middle component close to the free electron *g*-value and also of a rhombic nitrogen hyperfine coupling. The smallest *g*-value is significantly below g_e, and the highest significantly above g_e− both findings being in agreement with both species observed experimentally. The largest component of the ^{14}N HFC is calculated to be 86 MHz, and all components are predicted to be positive, which is due to the large value of the isotropic HFC. The two isomers **2** and **2′** show similar calculated EPR parameters and are therefore unlikely to represent the two experimentally observed species.

The calculated tensor orientations are shown in Figure 15. The smallest **g**-tensor component is significantly tilted from the Fe−N bond direction by 48 and 11° of the N−O bond direction while the largest component is almost perpendicular to the Fe−N−O plane. Experimentally this orientation is not known for **2**

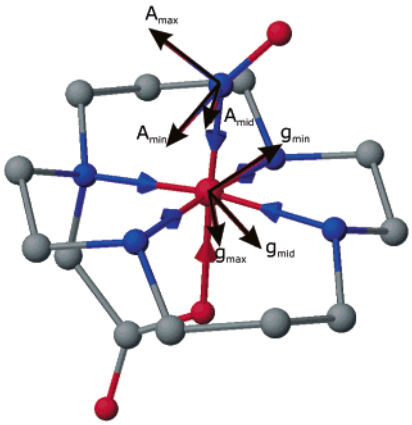

Figure 15. Predicted orientation of the **g**-tensor and the nitrogen hyperfine tensor in $[Fe(cylcam\text{-}acetate)(NO)]^+$ from B3LYP DFT calculations.

but we can make a comparison to the single-crystal EPR experiments on six-coordinated ferrous-myoglobin NO where a similar pattern of *g*-value orientations has been observed.[55] In particular, the largest component was found to be roughly perpendicular to the Fe−NO plane and the smallest component is within 10° of the N−O bond direction, precisely as in our calculations and those of Patchkovskii and Ziegler.[45]

The largest component of the nitrogen hyperfine coupling is perpendicular to the N−O bond, which is expected on the basis of the shape of the SOMO (Figure 12) which shows that the π^*_σ orbital has its lobes oriented along this direction which will give rise to a large positive spin density field gradient along the lobe direction. The large positive isotropic hyperfine coupling is noteworthy because it shows that upon bending of the Fe−NO unit some 2s character is mixed into the NO-π^* manifold (2.7% in the calculations) which is enough to dominate over the core polarization contribution which would give a negative contribution to the nitrogen HFC. The calculated orientation of the largest ^{14}N HFC component is mainly along g_{mid} from which it deviates by ∼21°. Thus, in agreement with experiment, the largest hyperfine splitting is predicted to occur along the g_{mid} direction but due to the tilting it will not reach its maximum value. The corrected value cos(21) × 86 MHz ≈ 80 MHz agrees reasonably well with the coupling of ∼74 MHz read off the experimental spectrum and gives some confidence in the spin distribution calculated by the B3LYP method.

The calculated ^{57}Fe HFC parameters are also shown in Table 10 but are thought to be less reliable due to the systematic errors in present day nonrelativistic DFT methods.[42,56,57] Nevertheless, the calculated ^{57}Fe HFC shows a large ansiotropy and a small A_{iso} value. Both results are consistent with the experimental observations and are due to the limited spin density at the iron and small **g**-tensor rhombicity. However, the calculated ^{57}Fe HFC tensor is clearly not highly accurate as evidenced by the wrong sign of the isotropic contribution and the error of up to a factor of ∼2 in the individual components.

We have performed a detailed analysis of the contributions to the **g**-tensor, which is documented in the Supporting Information. From this analysis we conclude that the *g*-shifts are to roughly equal extents caused by the SOC contributions due to the iron despite the limited iron spin density and the SOC that occurs between the two NO-based π^* orbitals (Figure S4). Importantly, any model that tries to explain the **g**-tensor based on the $(\pi^*)^1$ configuration alone is unrealistic since it neglects the important covalency contributions due to the metal.[58] In addition we have calculated the *g*-shifts as a function of the Fe−NO bond angle (Figure S5) and have found a pronounced dependence of the g_{min} and g_{max} shifts which can be mainly traced back to the steep variation in the $\pi^*_\sigma \rightarrow \pi^*_v$ excitation energy. Thus, the minimal and maximal **g**-tensor components become much more prone to *g*-strain effects caused by microheterogeneity in the Fe−NO bond angle (which is a soft mode), which helps to explain the difficulty to obtain high-quality spectra at high microwave frequencies.

Conclusions

Potentially, the nitrosyl ligand can coordinate in the four possible states NO^+ ($S_{NO} = 0$), $NO^\bullet$ ($S_{NO} = 1/2$), NO^- ($S_{NO} = 0$), and NO^- ($S_{NO} = 1$). In iron nitrosyl complexes these states could be coupled to either Fe(II) ($S_{Fe} = 0$, 1, or 2), Fe(III) ($S_{Fe} = 1/2$, 3/2, or 5/2) or perhaps Fe(IV) ($S_{Fe} = 1$, 2) centers thus leading to a large variety of different electronic situations each of which will be associated with a distinctive reactivity. Thus, in order to address these issues in the context of, e.g, enzymatic reaction mechanisms, it is important to experimentally and theoretically establish the correct electronic structure description in series of low-molecular weight model complexes. This work has been performed with the main objective to obtain an experimentally calibrated bonding picture in a concise series of synthetic non-heme iron nitrosyl complexes in the low-spin $\{FeNO\}^6$ ($S = 0$), $\{FeNO\}^7$ ($S = 1/2$), and $\{FeNO\}^8$ ($S = 0$) states. The $\{FeNO\}^6$ and $\{FeNO\}^7$ species (**1** and **2**) with the ligand system cyclam-acetate are structurally and spectroscopically fully characterized. The confident assignment of the corresponding $\{FeNO\}^8$ species is based on the spectroscopic characterization coupled to detailed calculations. Considerable insight into the physical properties and the bonding in these complexes was achieved by closely matching the experimental observables (structures, vibrational frequencies, Mössbauer parameters, EPR parameters) to DFT calculations. In addition to validating the theoretical approach the calculations provide a unified picture of the electronic structure of low-spin non-heme iron nitrosyls in perhaps unprecedented detail. Thus, in our interpretation the redox steps in the series are essentially ligand centered leading to $NO^+ \rightarrow NO^\bullet \rightarrow NO^-$ ($S_{NO} = 0$) while the central iron remains in the low-spin Fe(II) state throughout. This does not mean, however, that the iron is unaffected by the redox chemistry that is going on at the ligand. The main effect that we have identified is that the back-bonding ability of the NO ligand interaction varies dramatically along the series ranging from extremely strong (NO^+) to relatively weak (NO^-). This reduction leads to the pronounced changes of the Mössbauer parameters that locally probe the electron density around the iron center. On the other hand, the essentially ligand-centered redox steps explain the trends in the vibrational data as well as the EPR results.

For the $\{FeNO\}^6$ and $\{FeNO\}^7$ species this description is consistent with other studies on similar systems. In particular

(55) (a) Hori, H.; Ikeda,-Saito, M.; Yonetani, T. *J. Biol. Chem.* **1981**, *256*, 7849. (b) Kappl, R.; Hüttermann, J. *Isr. J. Chem.* **1989**, *29*, 73.
(56) Munzarova, M. L.; Kaupp, M. *J. Phys. Chem. A* **1999**, *103*, 9966.
(57) Neese, F.; Solomon, E. I. In *Magnetoscience-From Molecules to Materials*; Miller, J. S., Drillon, M., Eds.; Vol. IV, pp 345−466.
(58) McGarvey, B. R.; Ferro, A. A.; Tfouni, E.; Bezerra, C. W. B.; Bagatin, I.; Franco, D. W. *Inorg. Chem.* **2000**, *39*, 3577.

the careful study of Grohmann and co-workers[9] came to a similar conclusion on the basis of closely related spectroscopic measurements coupled to DFT calculations.[9] Likewise, the present results are consistent with the descriptions that Olabe and co-workers have given of the $[Fe(CN)_5(NO)]^{2-,3-,4-}$ series[13] from calculations and the experimental results of Mascharak and co-workers on a non-heme iron nitrosyl system.[14]

The finding of ligand-centered oxidation steps is of importance for the interpretation of the mechanisms of enzymes dealing with NO. Among others, some prominent iron enzymes are the CCNIR, the cd_1 nitrite reductase, the cytochrome P450 NO reductase, a non-heme iron NO reductase, hydroxylamine oxidoreductase, nitric oxide synthase, or guanylate cyclase all described in recent papers and reviews.[15,46,59] Most of these enzymes contain heme iron. However, in view of the fact that the metrical details of NO binding to heme and non-heme iron centers as well as their spectroscopic properties are exceedingly similar,[46] we believe that most of the conclusions that we have reached in this study are also valid in low-spin heme iron nitrosyl systems. For example, in the case of CCNIR we have recently proposed that the $\{FeNO\}^6 \rightarrow \{FeNO\}^7 \rightarrow \{FeNO\}^8$ cascade occurring at a lysine ligated heme iron active site is part of the catalytic mechanism.[15] The ligand-centered redox steps would have the dual role of increasing the nucleophilicity of the NO ligand to make it prone to subsequent protonation as well as lowering the strength of the NO bond to activate it for subsequent cleavage. Furthermore, since the central iron stays in the low-spin Fe(II) form throughout the catalytic cycle, no spin state changes which could interfere with efficient kinetics are required and the whole reaction could cleanly proceed on a single potential energy surface.[15]

We hope that furthering the understanding of non-heme iron nitrosyl systems in the way addressed in this paper will give even more insight into bioinorganic reaction mechanisms in future investigations.

Acknowledgment. This work was financially supported by the Max-Planck Society, the Fonds der Chemischen Industrie, and the Deutsche Forschungsgemeinschaft which is gratefully acknowleged. We also thank Dr. Leonardo Slep and Dr. Taras Petrenko for helpful discussions. C.A.G. is grateful for an A. v. Humboldt fellowship.

Supporting Information Available: Listings of crystallographic details, atom coordinates, bond lengths, and bond angles, thermal displacement parameters, and calculated positional parameters of hydrogen atoms for complexes **1** and **2** (Tables S1−S10), details of EPR simulation procedures (Table S11), zero-field Mössbauer spectra for **1**−**3** (Figure S1), an MO scheme for $\{FeHNO\}^8$ (Figure S2), correlation of bond length and stretching frequency for small $N_xO_yH_z$ species (Figure S3), and a model for the EPR **g**-tensor in **2** (Figures S4 and S5). This material is available free of charge via the Internet at http://pubs.acs.org.

JA030645+

(59) (a) Brown, R. L.; Radford, H. E. *Phys. Rev.* **1966**, *147*, 6−12. (b) Margenau, H.; Henry, A. *Phys. Rev.* **1950**, *78*, 587−592. (c) Beringer, R.; Castle, J. G. *Phys. Rev.* **1950**, *78*, 581−586.

(60) (a) Wasser, I. M.; de Vries, S.; Moënne-Loccoz, P.; Schröder, I.; Karlin, K. D. *Chem. Rev.* **2002**, *102*, 1201. (b) Ford, P. C.; Lorkovic, I. M. *Chem. Rev.* **2002**, *102*, 993. (c) Einsle, O.; Messerschmidt, A.; Stach, P.; Bourenkov, G. P.; Bartunik, H. D.; Huber, R.; Kroneck, P. M. H. *Nature* **1999**, *400*, 476. (d) Daiber, A.; Nauers, T.; Takaya, N.; Kudo, T.; Weber, P.; Hultschig, C.; Shoun, H.; Ullrich, V. *J. Inorg. Biochem.* **2002**, *88*, 343. (e) Silaghi-Dumitrescu, R. *Eur. J. Inorg. Chem.* **2003**, *6*, 1048.